ELEMENTA
Science of the Anthropocene

Shupe, MD, et al. 2026. The two radiative states of the Arctic atmosphere and their impacts on the surface energy budget of sea ice. *Elem Sci Anth*, 14: 1. DOI: https://doi.org/10.1525/elementa.2025.00100

RESEARCH ARTICLE

# The two radiative states of the Arctic atmosphere and their impacts on the surface energy budget of sea ice

Matthew D. Shupe[1,2,3,*], P. Ola G. Persson[1,2,3], Christopher J. Cox[2], Michael R. Gallagher[1,2,3], Amy Solomon[1,2,3], Anne Sledd[1,2,3], Byron Blomquist[1], Ian M. Brooks[4], David Costa[1,2], Jackson Osborn[2], Don Perovich[5], Laura D. Riihimaki[1,6], and Taneil Uttal[2,†]

The surface energy budget (SEB) is a central regulator of Arctic climate and sea ice evolution, yet its processes remain poorly constrained due to sparse observations and complex, coupled surface-atmosphere interactions. This study leverages year-long measurements from the Multidisciplinary drifting Observatory for the Study of Arctic Climate (MOSAiC) to provide the most comprehensive assessment to date of the central Arctic SEB and its modulation by atmospheric variability. Ship- and ice-based observations from October 2019 to September 2020 were used to directly measure or tightly constrain each term of the SEB, leading to exceptional energetic closure with the seasonal snow and ice mass balance. The analysis reveals strong seasonal transitions in atmosphere-surface energy transfer that are modulated by the atmospheric state and constrained by the ability of the surface temperature to respond. Classification of the atmosphere into its two dominant radiative states—the semi-transparent (ST) and opaque (OP)—highlights the central role of synoptic-scale variability in clouds. The ST atmospheric state dominated the long winter ice growth season, with limited cloudiness supporting persistent surface radiative cooling and ice growth. The OP state, associated with liquid-containing or thick ice clouds, became dominant in spring, with the combination of increased solar heating and cloud surface longwave warming driving ice and snow melt. Eddy covariance versus bulk approaches for deriving surface turbulent heat fluxes provide vastly different perspectives on the role of turbulence in modulating the SEB. These results establish a high-quality benchmark dataset for Arctic SEB studies and demonstrate how the balance of atmospheric radiative states exerts a first-order control on the annual evolution of the sea ice. The findings have broad implications for advancing observing technologies, understanding Arctic amplification, improving climate models, and predicting future sea ice change.

**Keywords:** Arctic, Clouds, Energy budget, Sea ice, Atmosphere, MOSAiC

## 1. Introduction

Amplified temperature increases relative to lower latitudes and declining cryosphere are two signatures of shifts in the balance of energy at the Arctic surface, which are ultimately driven by changes in atmospheric composition and its associated dynamics. These systematic shifts modulate surface energy transfer through changes in surface type, thinning sea ice with decreased extent (Jenkins and Dai, 2021), modified near-surface temperature structure (Zhang et al., 2021), alterations in snowfall (Khani et al., 2022), adjusted interseasonal heat storage (Chung et al., 2021), and other energy regulation processes. Arctic change is also promoted by feedbacks (e.g., Stuecker et al., 2018; Hankel and Tziperman, 2021; Previdi et al., 2021; Wendisch et al., 2022), many of which are linked via the surface energy budget (SEB). An understanding of Arctic change thus requires understanding the SEB and its key modes of variability.

The SEB represents the thermodynamic processes through which the atmosphere interacts with the surface. It is important for all Arctic surface types, most of which

[1] Cooperative Institute for Research in Environmental Sciences, University of Colorado, Boulder, CO, USA
[2] Physical Sciences Laboratory, National Oceanic and Atmospheric Administration, Boulder, CO, USA
[3] National Snow and Ice Data Center, University of Colorado, Boulder, CO, USA
[4] School of Earth and Environment, University of Leeds, Leeds, UK
[5] Thayer School of Engineering, Dartmouth College, Hanover, NH, USA
[6] Global Monitoring Laboratory, National Oceanic and Atmospheric Administration, Boulder, CO, USA
[†] Retired.
* Corresponding authors:
Emails: matthew.shupe@colorado.edu; matthew.shupe@noaa.gov

are sensitive to energetic changes, but here we focus on the sea ice. The net energy flux density at the air-ice interface is defined as:

$$F_{\mathrm{sfc}} = F_{\mathrm{atm}} + C = Q_{\mathrm{net}} - H_s - H_l + C, \quad (1)$$

where $F_{\mathrm{atm}}$ is the total atmospheric flux at the interface (positive into the surface); $C$ is the upward conductive heat flux to the surface from below; $H_s$ and $H_l$ are the upward turbulent sensible and latent heat fluxes away from the surface, respectively; and $Q_{\mathrm{net}}$ is the net broadband irradiance at the surface given as:

$$\begin{aligned} Q_{\mathrm{net}} &= \mathrm{SWD} - \mathrm{SWU} + \mathrm{LWD} - \mathrm{LWU} \\ &= \mathrm{SWD}(1-\alpha) + \mathrm{LWN}, \end{aligned} \quad (2)$$

where SW and LW are shortwave and longwave irradiances, respectively; D, U, and N represent downward, upward, and net irradiances, respectively; and $\alpha$ is the surface albedo. Transmission of solar energy by the surface is addressed below. Note: All variables and parameters included in this article are summarized in Appendix A.

For an infinitesimally thin, massless surface interface, $F_{\mathrm{sfc}}$ is the "balance" of energy exchange processes at the surface. However, typically Equation 1 is considered the "budget" of a layer with finite depth and mass, where $F_{\mathrm{sfc}}$ relates to changes in the layer's temperature and/or mass. If the interface is defined as the full layer of snow and sea ice covering the Arctic Ocean, one can consider the net energy budget of that interface layer as:

$$F_{\mathrm{net}} = F_{\mathrm{sfc}} + F_{\mathrm{bot}} = \Delta U - \Delta M, \quad (3)$$

where

$$F_{\mathrm{bot}} = F_{\mathrm{ocn}} - T_r - C_b, \quad (4)$$

and $F_{\mathrm{ocn}}$ is the upward ocean heat flux to the sea ice, $T_r$ is the downward transmission of solar energy through the ice into the ocean, and $C_b$ is the upward conduction of heat from the ice bottom. Conservation of energy and mass dictates that changes in $F_{\mathrm{net}}$ related to energy divergence or convergence within the snow-ice layer must equate to changes ($\Delta$) in the layer's internal energy or storage ($U$) or in its mass ($M$) via growth or melt. When $F_{\mathrm{net}}$ is positive, the snow-ice layer gains energy and warms until the melting point, after which excess energy goes into melt. When $F_{\mathrm{net}}$ is negative, the snow-ice layer loses energy and thus cools and grows more ice. For Arctic sea ice, growth typically only occurs at the bottom, while melt can happen at both the top and bottom. While the atmospheric temperature varies widely, the ocean immediately below the sea ice is in equilibrium with the ice and thus fixed at the freezing point of the ocean water. Conduction redistributes heat vertically through the ice and snow, linking $F_{\mathrm{sfc}}$ and $F_{\mathrm{bot}}$. $C$ and $C_b$ vary independently in response to variability in $F_{\mathrm{sfc}}$ and $F_{\mathrm{bot}}$ (e.g., Sledd et al., 2024), helping to determine the ice-snow thermal structure through complex interplay with the vertical distribution of solar energy and the changing profile of $U$. Over sufficiently long periods (months), conduction is the largest of these terms, such that $C$ and $C_b$ are nearly equal.

To quantify the evolution of the SEB requires understanding the drivers of variability in the terms that comprise Equations 1 and 2. Of the many transient modes of variability, perhaps the most impactful on the SEB, and least understood, is clouds. The presence or absence of clouds, and particularly those containing liquid water (e.g., Shupe and Intrieri, 2004), is a primary determinant leading to a bimodal distribution of surface LW radiation that defines the two dominant radiative states of the Arctic system (e.g., Stramler et al., 2011). These two states have been recognized over sea ice (Graham et al., 2017), over terrestrial land surfaces (Cox et al., 2012), and across the Arctic using satellite observations (Bertossa and L'Ecuyer, 2024). While largely driven by advection of large-scale moisture impacting clouds (Persson et al., 2017), the states are also influenced by low-level winds (Dahlke et al., 2025). Moreover, the states themselves extend beyond radiation to include co-variability in surface skin temperature, surface energy fluxes, and atmospheric structure (Stramler et al., 2011; Persson et al., 2017). This article focuses on the annual evolution of all components of the sea ice SEB and the influence of these two Arctic radiative states on that evolution.

Limited information exists on the SEB over sea ice. A comprehensive set of observations, extending over nearly a full annual cycle in the western Arctic sea ice, was obtained during the Surface Heat Budget of the Arctic Ocean (SHEBA) experiment in the late 1990s. At SHEBA (74–81°N), Persson et al. (2002) found a net annual surface energy surplus that was driven by greater incoming LW radiation than expected from models, partially mitigated by less solar radiation and weaker turbulent heat fluxes at the surface, leading to a net thinning of the multiyear sea ice that was typical of the western Arctic at that time. Similar measurements were made during shorter observational campaigns including the early spring Arctic Leads Experiment (LEADEX; Ruffieux et al., 1995), the Arctic Summer Cloud Ocean Study (ASCOS; Sedlar et al., 2011), the winter–spring Norwegian Young Ice expedition (N-ICE; Walden et al., 2017), and others. Some SEB components were also measured at periodic Russian drifting stations (Frolov et al., 2005), although with limited data availability it is unclear if the full SEB was estimated. The SEB, or its key components, has also been characterized at land-based stations surrounding the Arctic Ocean (Dong et al., 2010; Grachev et al., 2017; Miller et al., 2017), but it is unknown how representative these are of processes over the sea ice. Lastly, there have been efforts to derive surface radiative fluxes from pan-Arctic satellite observations (Zhang et al., 2004; Kato et al., 2011; Karlsson et al., 2017; Kato et al., 2018), typically with significant uncertainties due to their representation of, and assumptions about, surface and cloud properties (Riihelä et al., 2017; Huang et al., 2022). Satellite-based retrievals of Arctic surface turbulent heat fluxes have also been attempted (Boisvert et al., 2013), although evaluation against surface-based observations reveals a higher uncertainty than reanalysis output (Zhang et al., 2023), limiting their use for process understanding.

The spatiotemporal sparsity of SEB measurements over the Arctic sea ice is due to limitations in accessibility, particularly in winter, and observational challenges in extreme conditions (e.g., Bourassa et al., 2013). These challenges have led to shortcomings in our understanding, quantification, and generalization of SEB processes that have implications for clarifying and modeling the drivers and feedbacks of the changing sea ice. To address important questions related to linkages between sea ice decline and lower latitude weather and climate (e.g., Dai and Song, 2020; Francis and Vavrus, 2021), it is essential that models can successfully represent SEB processes and their changes (Yu et al., 2024).

Despite its clear importance, models struggle to represent many of the fundamental features of the SEB and its variability over sea ice, and particularly the distinction of the primary radiative states of the Arctic system linked to cloudiness. For example, poor representation of clouds is associated with biased surface radiation and temperature in reanalyses (Engström et al., 2014), regional climate models (Tjernström et al., 2008), and forecast models (Solomon et al., 2023). Additionally, most global climate models evaluated as part of the 5th and 6th Climate Model Intercomparison Projects failed to produce a bimodal distribution of LWN at the Arctic surface or the appropriate relationship with near-surface stability (Pithan et al., 2014; Duffey et al., 2025). These failures were typically related to underrepresented cloudiness and thus overestimated surface cooling, which modifies the near-surface atmospheric stability, turbulent heat fluxes, and more (e.g., Svensson and Karlsson, 2011; Barton et al., 2014). In line with these issues, some models have compensating errors in SEB terms (e.g., $H_s$ or $C$) that account for the deficits left by weaknesses in simulating clouds (Sorteberg et al., 2007; Pithan et al., 2014; Sedlar et al., 2020; Solomon et al., 2023; Sledd et al., 2025). Several studies found seasonal dependencies in surface temperature errors, with the largest biases in winter, but increasing influence from surface albedo errors in summer (Karlsson and Svensson, 2013; Boeke and Taylor, 2016). Collectively, these studies illustrate spatial, seasonal, and inter-model variability in relationships among errors in clouds, radiative fluxes, surface temperature, and other SEB components in large-scale models.

The Multidisciplinary drifting Observatory for the Study of Arctic Climate (MOSAiC) expedition was specifically designed to address crosscutting issues such as those related to energy transfer at the Arctic atmosphere—ice interface (Shupe et al., 2020). Based on and around the research vessel *Polarstern*, MOSAiC observations extended from October 2019 through September 2020. Over much of that time *Polarstern* drifted passively with the sea ice across the central Arctic, following the Transpolar Drift (85°N, 130°E to 79°N, 4°W). Sophisticated suites of instruments were operated onboard *Polarstern*, in a nearby sea ice camp, and in an autonomous Distributed Network surrounding *Polarstern*. The expedition explored physical, chemical, and biological processes that link the atmosphere, sea ice, snow, and ocean system in the central Arctic. Of specific use here are overview papers documenting the MOSAiC atmosphere (Shupe et al., 2022) and sea ice and snow (Nicolaus et al., 2022) research programs.

This article has two main goals. The first is to provide a detailed account of the SEB over sea ice during the MOSAiC year using arguably the highest-quality measurements in the central Arctic to date. Multiple important aspects of the SEB will be considered, including energetic closure with the sea ice and snow mass budget. The second goal is to explore the impacts and responses of this SEB to one of its primary drivers of variability, the clouds, by examining energetic influences of the two states of the Arctic atmospheric system.

## 2. Observations

### 2.1. Surface energy budget

Each term of the SEB was either directly measured or can be constrained by measurements at multiple locations during MOSAiC over most of the period from October 10, 2019, through September 21, 2020. The primary measurement location was the MOSAiC Central Observatory where the Met City site was operated on the sea ice at distances of 300–600 m from *Polarstern*. Additional measurements were made by semiautonomous systems operated within the MOSAiC Distributed Network (Rabe et al., 2024) at distances up to 23 km. It is important to keep in mind that all these observations drifted over time with the sea ice across the Arctic Ocean. Overall, these data represent a "sea ice Lagrangian" perspective, where passing atmospheric and oceanic processes interact with a region of sea ice that is followed over time. Spatial variability in all processes should be kept in mind. While most measurements and derived products have been introduced via dedicated publications, basic information will be summarized here.

Atmospheric flux measurements are described in detail, and evaluated, by Cox et al. (2023e). Surface measurements of broadband radiation were made with pairs of pyranometers (SWD, SWU) and pyrgeometers (LWD, LWU) at Met City and at 3 remote Atmospheric Surface Flux Stations (ASFSs) deployed across the Distributed Network called ASFS30, ASFS40, and ASFS50. At Met City, the upward- and downward-looking radiometers were located at approximately 1 m and 3 m above the surface, respectively. At the ASFS, all radiometers were mounted at a nominal height of 2 m above the surface. These broadband radiation measurements were used to derive the surface skin temperature ($T_{skin}$) using an assumed surface emissivity of 0.985 (Cox et al., 2023e). Additionally, the broadband surface albedo ($\alpha$) was derived using 1-day running averages of SWU divided by SWD. This running average window helped to mitigate diurnal impacts related to small offsets of the horizontal level of the radiometers or the observed surface. Surface net radiative fluxes are calculated as LWN = LWD − LWU and SWN = SWD (1 − $\alpha$), the latter of which is approximately equal to SWD − SWU.

Surface turbulent $H_s$ and $H_l$ were derived using the eddy covariance (EC) approach based on 20-Hz measurements from three-dimensional sonic anemometers and open-path rapid gas samplers resampled to 10-Hz. At Met

City, anemometers were mounted at nominal 2, 6, and 10 m heights on a meteorological tower, while the gas sampler was mounted at 2 or 6 m depending on season. At the ASFS, these sensors were mounted at 3.86 m above the surface. In parallel, a bulk flux approach (Andreas et al., 2010) was also used to derive turbulent heat fluxes from near-surface meteorological measurements. Temperature and relative humidity were measured at nominal heights of 2, 6, and 10 m on the Met City tower and at 2 m on the ASFSs, while pressure was measured at 2 m. All measurements were averaged to 10-min resolution and subjected to intensive quality control to ensure high quality and consistency across stations and among parameters. Detailed information on measurement conditions, data processing, corrections, calibrations, uncertainties, and quality assessments are provided by Cox et al. (2023e).

During periods with surface snow cover and prior to influence from solar radiation, $C$ up to the surface interface was calculated by Sledd et al. (2024) by solving a one-dimensional heat diffusion equation using temperature profile measurements through snow and ice from a collection of Seasonal Ice Mass Balance buoys (Perovich et al., 2023) and Snow and Ice Mass Balance Arrays (Lei et al., 2022). To represent the diversity of surface conditions, we use the mean near-surface $C$ ($\sim$6 cm depth) from all available systems, which could be as many as 13 at a given time. Vertically, the 6-cm depth was chosen to represent the value of $C$ at the "surface" yet avoid potential irregularities related to an exact identification of the surface in the measurements. The derived $C$ varied with atmosphere-induced changes in subsurface temperature (i.e., internal energy). However, when averaged over longer time periods such as the winter ice growth season, $C$ was nearly constant in the vertical. The variability of $C$ across the sites was typically small, with the mean standard deviation across available sites of 6.2 W m$^{-2}$ and 90% of the time the standard deviation was between 3 and 10 W m$^{-2}$.

After March 14, when sunlight complicated in ice temperature measurements, $C$ was calculated using a simple approximation (Maykut, 1978; Perovich et al., 2023) of:

$$C = g(T_{\mathrm{ocn}} - T_{\mathrm{skin}}), \tag{5a}$$

where

$$g = k_{\mathrm{i}} k_s / (k_s D_i + k_i D_s) \tag{5b}$$

and $k_s$ is the effective thermal conductivity of snow assumed to be 0.4 W m$^{-1}$ K$^{-1}$ based on average values across MOSAiC (Perovich et al., 2023; Sledd et al., 2024), $k_i$ is the thermal conductivity of bulk sea ice (2.0 W m$^{-1}$ K$^{-1}$), $D_i$ and $D_s$ are the sea ice and snow thickness, respectively, and $T_{\mathrm{ocn}}$ is the ocean temperature of $-1.8$°C based on many buoy measurements. The temporal evolutions of $D_s$ and $D_i$ are based on numerous independent physical measurements across the MOSAiC domain (Lei et al., 2022; Itkin et al., 2023; Perovich et al., 2023; Raphael et al., 2024) and are discussed in more detail later.

One additional term based on atmospheric measurements that can be seasonally important for the full sea ice energy budget is the transmission of solar energy through the sea ice into the ocean, given as (Light et al., 2008; Persson, 2012):

$$T_r = I_o \ \mathrm{SWN}\, e^{-K_s D_s}, \tag{6a}$$

$$T_r = \mathrm{SWN}(f_v I_v e^{-K_{iv} D_i} + f_n I_n e^{-K_{in} D_i}), \tag{6b}$$

where the first equation represents snow transmission during periods when significant snow was present (through May 5) and the second equation represents snow-free ice transmission with visible (350–700 nm) and near-infrared (700–3,000 nm) contributions. $D_s$ is snow depth, $I_o$ is the snow surface transmission parameter (0.3), and $K_s$ is the snow solar extinction coefficient, assumed to be 16 m$^{-1}$ until May 5 after which it declines linearly to 3 m$^{-1}$ when there is no snow remaining on flat ice. $D_i$ is the ice thickness, $I_v$ and $I_n$ are the ice surface transmission parameters for visible (0.95) and near-IR (0.37) radiation, $K_{iv}$ and $K_{in}$ are the extinction coefficients for visible (0.72 m$^{-1}$) and near-IR (4.6 m$^{-1}$) radiation, and $f_v$ and $f_n$ are the weightings for visible (0.60) and near-IR (0.40) radiation. While this formalism is consistent with past research, here the overall transmission is scaled by a factor of 2 to match the cumulative broadband solar flux transmitted through the base of the sea ice of 20 MJ m$^{-2}$ determined by Perovich et al. (2025) for July 11, 2020, at MOSAiC.

Over the course of the MOSAiC year, each SEB station faced unique operational challenges that caused gaps in the time series. These included power outages at Met City due to local ice dynamics, polar bear damage, interruptions in most operations for movements of *Polarstern*, and the destruction of ASFS40 in an ice ridging event (see Cox et al., 2023e). For use here, the observations have been combined to produce the most continuous and consistent dataset possible to represent the MOSAiC sea ice domain. When available, observations from Met City were used as the default since these were attended and monitored daily. During mid-May through late June 2020, when *Polarstern* left the MOSAiC ice floe for resupply, Met City was replaced by ASFS30 to continue measurements at that location. Similarly, for July (ASFS50) and late August to September (ASFS30 and ASFS50), ASFS systems were installed within 200–300 m of Met City and were used to fill any gaps. For infrequent observational gaps at Met City that did not have a proximal ASFS, observations were used from an ASFS deployed within the Distributed Network (i.e., within 10–23 km). While there can be differences in SEB parameters across these scales, they are generally found to be small relative to measurement uncertainty for time periods when simultaneous data exist (see Supplement Text T1), particularly when considered over the averaging periods used to conduct the analyses here. During the first 3 weeks of August, *Polarstern* was repositioned northward, during which time no SEB measurements were available leaving a general gap in the record. Finally, gaps in derived turbulent heat fluxes from EC measurements were filled using bulk turbulent heat fluxes that were bias-corrected relative to available EC fluxes over running 6-day windows. A comparison between the EC and bulk approaches is included in

Section 4.2 to demonstrate key points about turbulent heat fluxes.

Observing stations were mostly deployed on level, second-year sea ice and therefore largely represent the conditions over sea ice floes with occasional influence from nearby leads or open water on some parameters. However, these observations do not always represent wider spatial domains, particularly when they include a large fraction of open water. Additionally, while the SEB measurements from October 2019 through July 2020 were all made of the same drifting region of sea ice, once that ice reached the ice edge in Fram Strait, *Polarstern* was repositioned to a new location in the sea ice near the North Pole to complete the year from late August through mid-September.

Despite the various challenges in creating the SEB dataset, it is the most comprehensive and accurate representation of the SEB constructed over the Arctic sea ice. Past SEB datasets over Arctic sea ice have suffered from numerous, and sometimes unquantified, instrumental challenges related to instrument icing affecting radiation measurements and inhibiting direct measurements of turbulent heat fluxes (e.g., Persson et al., 2002) or included only short and/or interrupted time series (e.g., Ruffieux et al., 1995; Sedlar et al., 2011; Walden et al., 2017; Nilsson et al., 2021). Satellite estimates are limited in what they can provide over sea ice, with significant uncertainties for terms like the turbulent or conductive heat fluxes (e.g., Zhang et al., 2023).

### 2.2. Cloud measurements

To examine the causes of variability in the SEB, several additional measurements and products were used to characterize the atmospheric meteorological state and clouds. Cloud properties including time-height information on cloud phase, ice water content (IWC), and liquid water content (LWC) were derived using the ShupeTurner cloud retrieval algorithm (Shupe et al., 2015; Shupe, 2022). This retrieval incorporated measurements made onboard *Polarstern* from a Ka-band ARM Zenith Cloud Radar (Johnson et al., 2022), W-band ARM Cloud Radar (Wang et al., 2022), Vaisala ceilometer (Zhang et al., 2022), depolarization Micropulse Lidar (Sivaraman et al., 2022), two microwave radiometers (Ebell et al., 2022; Zhang, 2022), and 6-hourly radiosondes (Maturilli et al., 2021). The microwave radiometers were used to derive a continuous series of the column-integrated liquid water path (LWP) and precipitable water vapor (PWV) wherein the Zhang (2022) product was the primary dataset, and the Ebell et al. (2022) dataset was bias adjusted and used to fill gaps. Ice water path (IWP) is the vertical integral of IWC. Cloud occurrence fraction was calculated by requiring the identification of significant cloud signal in at least two consecutive 30-m radar range gates to ensure that spurious noise did not impact the cloud fraction. The occurrence fractions of liquid or ice in any type of cloud in the vertical column, and as a function of height, were also determined. The cloud product was derived at 1-min resolution and averaged to 10 min to match the SEB data. This MOSAiC cloud product was evaluated using a radiative transfer closure analysis with surface and top-of-atmosphere radiative fluxes (Barrientos-Velasco et al., 2025), showing good closure statistics consistent with a similar analysis conducted using the same ShupeTurner product derived over northern Alaska (Shupe et al., 2015), lending confidence in the product. These cloud and atmosphere measurements were made onboard *Polarstern* and were therefore not collocated with the SEB measurements during the period of mid-May through late June when *Polarstern* transited out of the ice for a resupply.

## 3. The Arctic atmospheric states

### 3.1. State characteristics

The two primary radiative states of the Arctic atmosphere-surface system have been discussed previously (e.g., Shupe and Intrieri, 2004; Stramler et al., 2011; Cox et al., 2012; Graham et al., 2017; Persson et al., 2017; Bertossa and L'Ecuyer, 2024; Dahlke et al., 2025). These states are illustrated at MOSAiC via the distribution of observed surface LWN (**Figure 1a**). The bimodal nature of this distribution is apparent, with a distinction between modes at $-25$ W m$^{-2}$. The mode with LWN less than $-25$ W m$^{-2}$ represents the "optically thin" or "semi-transparent" state (hereafter ST), wherein emission from the surface to the atmosphere is significant and atmospheric emission down to the surface is much less due to low atmospheric emissivity. Alternatively, the mode with LWN greater than $-25$ W m$^{-2}$ represents the radiatively "opaque" state (hereafter OP), with much larger downward atmospheric emission that is closer in magnitude to the surface emission. In this state, the atmosphere and surface are more nearly in LW radiative equilibrium. The distinction between the states is thus due to differences in the balance of atmospheric versus surface emission, which are determined by the vertical structures of atmospheric opacity and temperature.

While the two states are typically well-defined in winter when solar radiation is limited in the Arctic, the distinction based on LWN occurs year-round. Here, the seasons are defined according to 7-day running average near-surface temperature (e.g., Shupe et al., 2022), with winter consistently colder than $-20$°C, summer consistently warmer than about $-2$°C, and spring and fall being the transitions between. As such, these seasons have different occurrence fractions (**Figure 1**, **Table 1**) but represent distinct regimes in terms of cloud and atmosphere properties (e.g., Figure S4). The modal LWN values of each state vary with season, as does the relative partitioning of occurrence between the states (**Table 1**, **Figure 1a**). For the OP state, the modal value ranges seasonally between $-10$ and $-4$ W m$^{-2}$, with most values being weakly negative because emission from cloudy atmospheres is less than from the surface due to a combination of temperature (cloud colder than surface) and/or cloud emissivity (emissivity less than unity) considerations. For most seasons, positive LWN is infrequent (4% of the time) because the surface can warm in response to atmospheric emission, diminishing radiative imbalances between the atmosphere and surface. Most occurrences of positive LWN are in summer (29% of the time), when warm atmospheric advection can bring optically thick clouds with

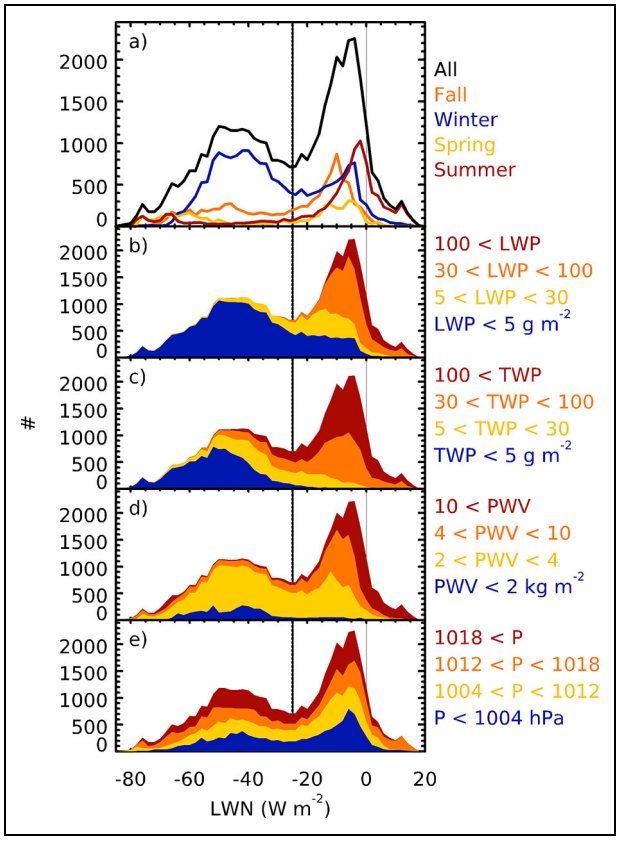


**Figure 1. Partitioned distributions of surface net longwave radiative flux.** The distribution of net longwave radiative flux (LWN), in counts per bin, for the full MOSAiC year partitioned in multiple ways: (a) The full year distribution (black) and other seasons (colors), defined according to Shupe et al. (2022) as Fall (September 6 to November 27), Winter (November 28 to April 13), Spring (April 14 to May 27), and Summer (May 28 to September 5). Other panels include the full year distribution broken down by contributions from cases with different ranges of (b) liquid water path (LWP), (c) total water path (TWP = LWP + IWP), where IWP is the ice water path, (d) precipitable water vapor (PWV), and (e) surface atmospheric pressure (*P*). The ranges for each color are given to the right of each panel. The LWN bin width is 2 W $m^{-2}$.

temperature >0°C while the sea ice cannot warm beyond its melting point. This condition, along with higher average cloud emissivity, also explains the higher summer modal value for the OP state. The ST state is most clearly defined in winter because it is the only season in which this state occurs more often than the OP state. The modal value of this broad winter distribution is nearly 40 W $m^{-2}$ less than that for the OP state. Fall shows a similar distribution with less frequent occurrence of the ST state. In spring and especially summer, the ST state occurs much less frequently than the OP state, and both seasons show modal values less than −60 W $m^{-2}$. This shift in warm-season LWN values is consistent with the temperature-dependence of the ST peak observed by Stramler et al. (2011). It is due to the diminished occurrence of surface-based temperature inversions during the ST state in summer relative to winter, which outweighs the effect of a moister atmosphere in summer. Overall, the annual difference between the OP and ST modal values exceeds 40 W $m^{-2}$. Since the decadal decline in Arctic sea ice can be explained by an energy imbalance of approximately 1 W $m^{-2}$ (Kwok and Untersteiner, 2011), processes that control the fractionation between states can be consequential.

MOSAiC observations provide a detailed perspective on the characteristics of these two states that builds on the observations of Graham et al. (2017), from a similar region but only part of the year, and Shupe and Intrieri (2004), for an annual cycle in the western Arctic sea ice. Dahlke et al. (2025) provide further analysis of these states during MOSAiC winter, including related wind conditions. Several key cloud and atmospheric quantities drive, or respond to, the two atmospheric states (**Figures 1**–**3**, S8, S9, **Table 2**). Importantly, the occurrence of liquid water-containing clouds is the clearest determinant (Shupe and Intrieri, 2004). When the distribution of LWN is partitioned by cloud LWP (**Figures 1b**, **2a**, S9b), nearly all occurrences of optically opaque clouds (LWP > 30 g $m^{-2}$) are found within the OP state, while only a few cases of thin liquid water clouds (5 < LWP < 30 g $m^{-2}$) occur in the ST state. This result is unsurprising considering differences in instrument viewing geometry and that the uncertainty in derived LWP is about 20 g $m^{-2}$ (Turner et al., 2007), which also leads to an appropriate amount of derived negative LWP values (which are clearly nonphysical). On the other hand, cases with no appreciable liquid water (LWP < 5 g $m^{-2}$) comprise the vast majority of the ST state. However, there are OP cases with no liquid water but particularly thick layers of cloud ice (also observed by Miller et al., 2015; Bertossa and L'Ecuyer, 2024). This point is borne out via the total water path (TWP = LWP + IWP). The OP state essentially always has at least 5 g $m^{-2}$ of condensed mass in the vertical column (**Figure 1c**). On the other hand, the ST state can exist even with a large IWP (**Figure 2b**), which in this case would be distributed over a deep layer with a low concentration of large ice crystals.

These points are further supported by examining cloud occurrence statistics (**Figure 3**). The OP state shows a 100% cloud occurrence, with ice and liquid in the vertical column 87% and 79% of the time, respectively. The ST state is not necessarily free of condensed mass. In this state, active sensors identified clouds composed of mostly ice 74% of the time, with liquid water 15% of the time, although usually with LWP less than the retrieval uncertainty (**Table 2**). Vertical profiles of cloud phase types show the typical profile of Arctic cloud occurrence with ice extending up to 8–9 km, a uniform cloud ice occurrence fraction from 2 to 5 km, and a steep increase in ice occurrence below 2 km. Liquid water occurs most frequently below 1 km but can extend up to 5 km or more (e.g., Shupe, 2011). Each atmospheric state has similar profiles but with markedly larger fractions for the OP relative to the ST state.

**Table 1. Fractional occurrence and modal value for the ST and OP states as a function of season**

| | Semi-Transparent (ST) | | Opaque (OP) | | LWN > 0 W m$^{-2}$ [a] | Season[b] |
|---|---|---|---|---|---|---|
| Subset | Fraction (%) | Mode (W m$^{-2}$) | Fraction (%) | Mode (W m$^{-2}$) | Fraction (%) | Fraction (%) |
| Total | 48 | −50 | 52 | −4 | 9 | 100 |
| Fall | 42 | −46 | 58 | −10 | 3 | 22 |
| Winter | 64 | −40 | 36 | −4 | 4 | 46 |
| Spring | 47 | −60 | 53 | −6 | 4 | 11 |
| Summer | 18 | −68 | 82 | −2 | 29 | 22 |

[a]Fractional occurrence of time that net longwave radiative flux (LWN) was greater than 0 W m$^{-2}$.

[b]Fraction of time occupied by each season. Seasons are defined as in Shupe et al. (2022).

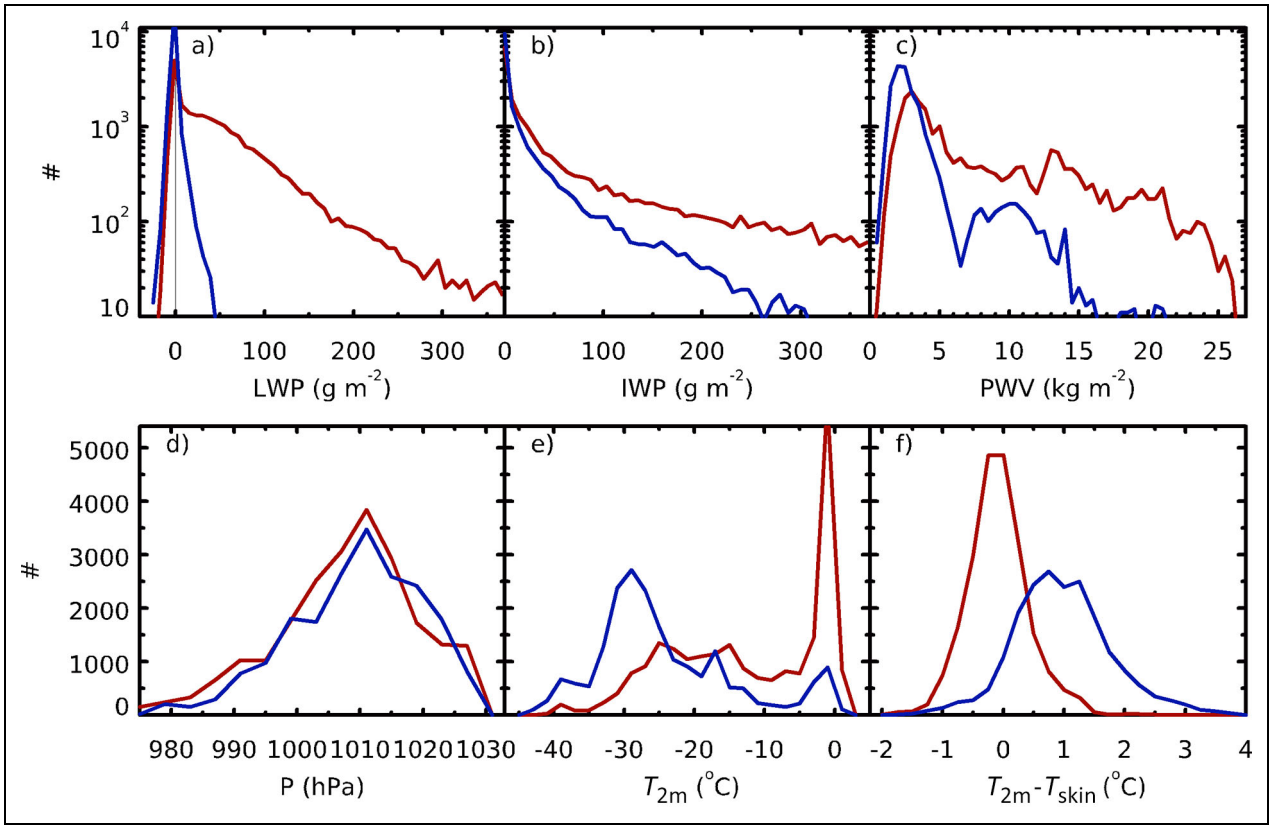


**Figure 2. Distributions of key parameters by atmospheric state.** Distributions, in counts per bin, of six parameters distinguished into the Opaque (red) and Semi-Transparent (blue) atmospheric states, including (a) liquid water path (LWP) and (b) ice water path (IWP), both with bin widths of 8 g m$^{-2}$, (c) precipitable water vapor (PWV) with bin width of 0.5 kg m$^{-2}$, (d) surface atmospheric pressure ($P$) with bin width of 4 hPa, (e) 2 m temperature ($T_{2\,m}$) with bin width of 2°C, and (f) near-surface temperature gradient, defined as the difference between 2 m and skin temperatures ($T_{2\,m} - T_{skin}$), with bin width of 0.25°C. Statistics exclude periods from mid-May through late June and early August when *Polarstern* was underway.

Water vapor also shows a general distinction between states (**Figure 2c**). Winter PWV is most often less than 5 kg m$^{-2}$ in the generally dry Arctic (Figure S9d). The PWV distribution during the ST state shows a relative increase in the lowest values compared to the OP state, while the OP state has values that can extend as high as 25 kg m$^{-2}$. However, the ST state can still be quite moist, with PWV values up to 15 kg m$^{-2}$ in summer. The near-surface temperature (**Figure 2e**) is somewhat warmer during the OP state, although these distributions are affected by differences in seasonal occurrence. Lastly, the near-surface temperature gradient (**Figures 2f**, S8b) indicates typically strong near-surface stability in the ST state as the surface efficiently cools leading to surface-based temperature inversions. The OP state is neutral near the surface with a mean near-surface temperature gradient of about 0 (e.g., Persson et al., 2002), consistent with radiative warming of the surface and possible near-surface mixing that may also be facilitated by clouds that are dynamically coupled to the surface (e.g., Brooks et al., 2017).

**Table 2. Mean and standard deviation (*SD*) of key parameters for the full dataset and the ST and OP atmospheric states[a]**

| | All | | Semi-Transparent (ST) | | Opaque (OP) | | |
|---|---|---|---|---|---|---|---|
| **Parameter** | **Mean** | ***SD*** | **Mean** | ***SD*** | **Mean** | ***SD*** | **Difference[b]** |
| $T_{2\ m}$ (°C) | −17.0 | 12.0 | −23.3 | 9.9 | −11.3 | 10.9 | 12 |
| $P_{2\ m}$ (hPa) | 1,011 | 11 | 1,011 | 10 | 1,010 | 11 | −1 |
| PWV (kg m$^{-2}$) | 6.0 | 5.4 | 3.5 | 2.7 | 8.2 | 6.1 | 4.7 |
| LWP (g m$^{-2}$) | 32 | 65 | 1 | 7 | 59 | 80 | 58 |
| IWP (g m$^{-2}$) | 64 | 145 | 20 | 49 | 104 | 185 | 84 |
| SWD (W m$^{-2}$) | 63 | 104 | 57 | 113 | 69 | 95 | 12 |
| LWD (W m$^{-2}$) | 219 | 61 | 172 | 36 | 261 | 47 | 89 |
| LWN (W m$^{-2}$) | −26 | 22 | −46 | 12 | −7 | 9 | 39 |

[a]Statistics exclude periods when *Polarstern* was underway.

[b]Difference of means between the OP and ST states.

Interestingly, while cloudiness is often associated with low-pressure systems, and indeed there was a relationship between surface pressure and LWN at SHEBA (Morrison et al., 2012), there was only a weak relationship at MOSAiC (**Figures 1e**, **2d**, S8c). LWN distributions for all four quartiles of surface pressure data are clearly bimodal and similar (**Figure 1e**). Upon more detailed examination of the relationship between these two variables, only at the lowest of pressures is there a slight preference for the OP state relative to the ST state (**Figure 2d**), which tends to occur mostly in the middle of winter (Figure S8c). This limited dependence on pressure at MOSAiC may be due to the diversity of regional circulation patterns, where the site was at many different locations relative to pressure centers. SHEBA occurred in the western Arctic where the typical Beaufort High varies primarily in magnitude but less in location.

To summarize, the OP state of the Arctic system is largely comprised of clouds containing liquid water, often supercooled, but can also include deep ice clouds. The ST state can be cloud free but also frequently includes ice clouds that have a vanishingly small impact on atmospheric radiation. The spread of values in each state is related to variations in cloud properties, fractional sky cover, water vapor amount, temperature structure, aerosol properties, and more. Additionally, while cloud properties are a strong determinant of the state, it is important to recognize that clouds typically occur within an air mass with enhanced atmospheric moisture and often increased temperature, as well as a modified boundary layer structure. Thus, the difference between the states is more than simply a "cloud radiative effect." Rather, it is more properly an "atmospheric state effect," with multiple interacting components. Finally, as conveyed in **Figure 1**, while the LWN distribution is clearly bimodal, there are intermediate states of the atmosphere with LWN values that are near the $-25$ W m$^{-2}$ value used to distinguish the states. Thus, this simple partitioning of the Arctic into two states should be considered within that context and care should be taken when applying such a concept to other locations.

### *3.2. Quantifying the atmospheric state effect*

The second primary goal of this work is to quantify the net effect of variability in clouds and the atmospheric state on the SEB and its components via what we define as the atmospheric state effect ($E$). Here, we simply distinguish the atmospheric states using the threshold of LWN $= -25$ W m$^{-2}$, which is the minimum between the two primary modes of the LWN distribution (**Figure 1**). The maximum $E$ on, or "forcing" of, a given parameter due to the OP atmospheric state is given as:

$$E(P) = P_{\mathrm{op}} - P_{\mathrm{st}}, \tag{7}$$

where $P_{\mathrm{op}}$ and $P_{\mathrm{st}}$ are the mean values of the parameter $P$ over the period of interest during the OP and ST states, respectively. However, to quantify the net atmospheric state effect ($E^*$), this maximum effect is multiplied by the fractional occurrence of the OP state over the time period ($A_{\mathrm{op}}$):

$$E(P)^* = \left(P_{\mathrm{op}} - P_{\mathrm{st}}\right)A_{\mathrm{op}}. \tag{8}$$

Thirty-day running windows are used to calculate time series of $E$ and $E^*$. This length of time was required to ensure sufficient statistical representation of each state within a given sampling window, while still preserving the important seasonal variations.

This approach is similar to the maximum cloud forcing approach employed by Walsh and Chapman (1998), with the addition of Equation 8 to arrive at the net effect, as introduced by Intrieri et al. (2002). One benefit to this approach, and the reason it is used here, is that it is a feasible way to examine the atmospheric state effect on all parameters of the SEB system and to develop a full accounting of the energetic changes that occur when the Arctic atmosphere shifts between relatively dry-clear versus moist-cloudy states. This way of considering the states and their radiative effect is distinct from past

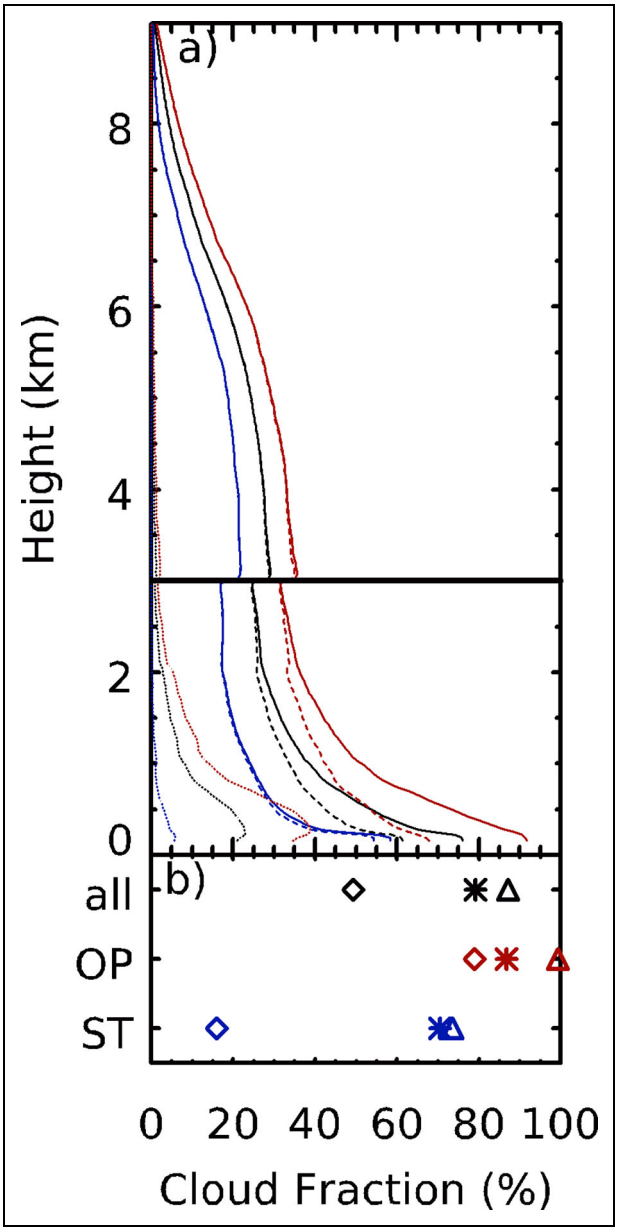


**Figure 3. Cloud occurrence and phase distinguished by atmospheric state.** (a) Profiles of occurrence fraction of any cloud (solid), cloud ice (dashed), and cloud liquid (dotted) for all time periods (black), the opaque state (OP, red), and the semi-transparent state (ST, blue). (b) Total values giving the fractional occurrence of all cloud (triangle), cloud ice (asterisk), and cloud liquid (diamond) as distinguished by atmospheric states. In panel (a) there is a discontinuity in the occurrence fractions at 3 km altitude where two distinct radar operational modes, with distinct sensitivities, are combined. Cloud occurrence fraction is inextricably linked to the sensitivity of the instruments used to observe it.

computations of, for example, cloud radiative forcing that often employ a model to compute an equivalent clear sky flux that is subtracted from the observed flux to determine the instantaneous role of clouds (e.g., Intrieri et al., 2002). There is not a readily feasible way to compute an equivalent clear sky flux for all SEB terms, and this type of approach only quantifies the hypothetical effect of clouds but does not include the concomitant variability of atmospheric moisture and temperature.

There are a few key aspects of this approach to discuss and justify. First, to more clearly delineate the effect of the OP state versus the ST state, one might define different boundaries between states, such as defining the ST state as LWN less than $-30$ W m$^{-2}$ and the OP state as LWN greater than $-20$ W m$^{-2}$. While this approach may be of interest to accentuate process differences between the states (e.g., Solomon et al., 2023), here we seek to represent all energy in the system and thus opt to employ a single threshold for distinguishing states, acknowledging the fact that there are intermediate conditions. Additionally, since LWN is used to classify the states, there may be an implied assumption that the LW radiative balance is the primary driver of variability in all terms of the SEB. While radiation is often the driver of SEB variability (e.g., Miller et al., 2017; Sledd et al., 2025), as explored below, there are other significant influences such as the roles of summer insolation or turbulent heat fluxes during strong wind events. Lastly, rather than using LWN, one might consider distinguishing the dataset based on the occurrence of clouds. However, there is no consistent definition of "cloud" to use for this purpose, as each instrument has its unique response to populations of condensed particles in the atmosphere, some of which are radiatively important while others are not. Thus, for these reasons, and due to the stark and compelling bimodality of LWN in the Arctic atmosphere, we use this parameter to identify and distinguish between the two states. As noted above (**Figures 1**–**3**), each state is comprised of a range of cloud and atmospheric conditions, while LWN is effectively a proxy for the net opacity of the atmosphere.

## 4. SEB over sea ice

Before examining the distinct roles of the two primary atmospheric states, we present the "best estimate" MOSAiC SEB. As noted in Section 2, this dataset combines multiple measurement systems to optimally address instrument issues and fill gaps to provide the most complete dataset possible.

### *4.1. SEB and its components*

The primary components of the SEB are displayed using 3-day running averages (**Figure 4**). This averaging window is used to smooth the highest frequency variability and more clearly reveal the general trends and relationships in the data that occur on synoptic time scales. An averaging window of this nature is also important because there are infrequent periods when data are combined from multiple sites that can be separated spatially, such that a longer time average mitigates small temporal differences among sites (see Supplement Text T1). Time series of daily-averaged values for individual energy budget terms, near-surface meteorology, and key cloud properties, along with monthly summary statistics, are also given in Supplement Text T2 and associated figures to provide information at different averaging scales.

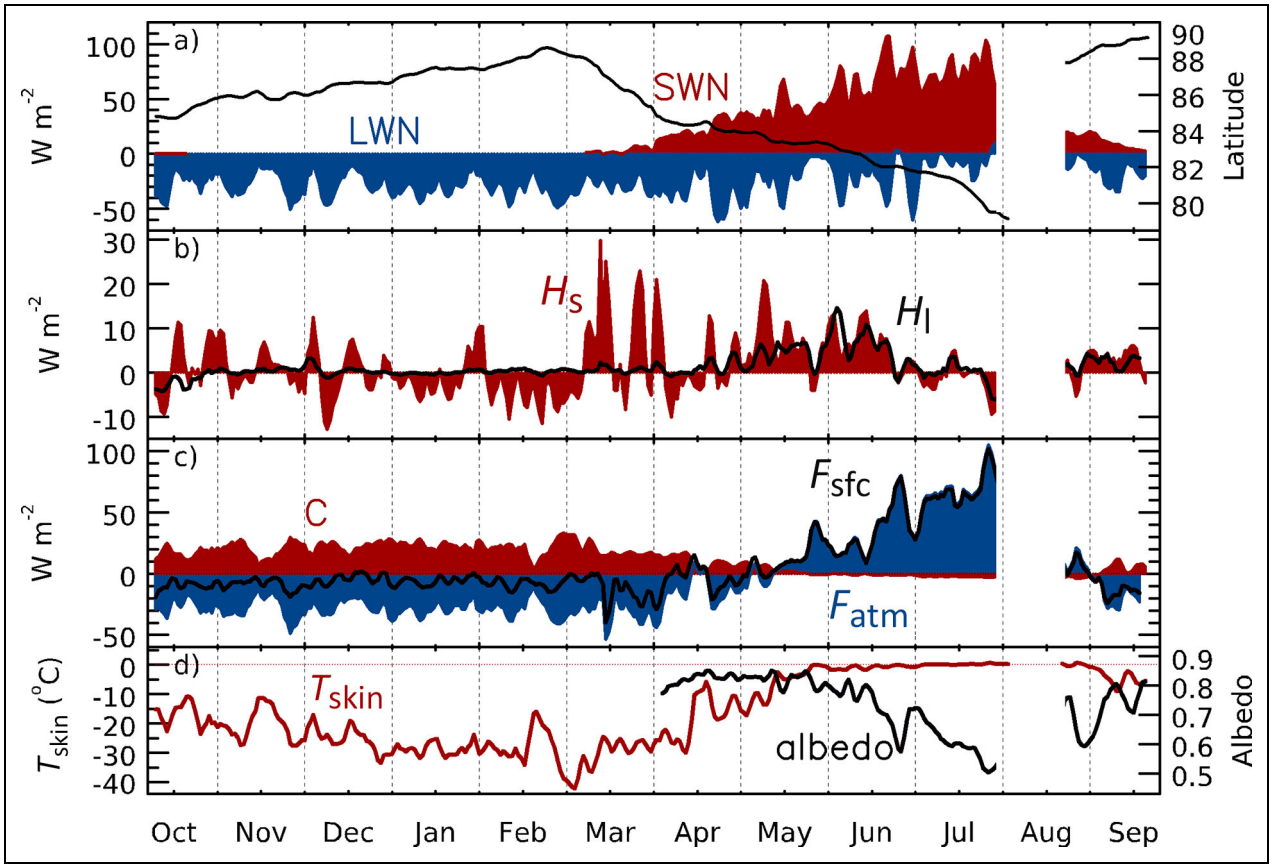


**Figure 4. Annual cycle of surface energy budget components.** Key components of the MOSAiC surface energy budget given as 3-day running means, including (a) net shortwave (SWN, red, left axis) and longwave (LWN, blue, left axis) irradiances and the latitude as context for the shortwave measurements (black line, right axis); (b) sensible ($H_s$, red) and latent ($H_l$, black) heat fluxes; (c) net atmospheric heat flux ($F_{atm}$, blue), which is balanced against the conductive heat flux ($C$, red) to result in the net surface energy budget ($F_{sfc}$, black line); and (d) the surface skin temperature ($T_{skin}$, red, left axis) and surface albedo (black, right axis).

One important seasonal reference that is both determined by the balance of SEB terms and influences three individual terms is the surface skin temperature (**Figures 4d**, S3a). First, the surface emission, that is, LWU, is directly related to $T_{skin}$ to the fourth power. Additionally, $T_{skin}$ is a boundary condition for the net temperature gradient through the sea ice, influencing $C$, and is a factor in the near-surface atmospheric temperature gradient, which influences $H_s$.

We introduce these data by describing the three basic phases of the skin temperature annual cycle—cooling, warming, and melting. Surface cooling started on August 30, 2020, and continued through the end of MOSAiC, with a short return to melt on September 13–14. Notably the location of these observations near the end of MOSAiC was on a different ice floe than the rest of the MOSAiC drift and at a different location relative to both the start and the end of that main drift, thus it is not clear when the cooling period started in the weeks prior to the initial start of MOSAiC. $T_{skin}$ decreased through the cold season despite periodic increases linked to warm air advection events and cyclones that occurred, for example, in mid-November and late February. The coldest temperature of −45°C was reached on March 4, 2020, a few days after the late February warm event when $T_{skin}$ reached −10°C. Thereafter, $T_{skin}$ warmed in steps, with a particularly significant warm air intrusion occurring in mid-April (e.g., Svensson et al., 2023), when the surface reached 0°C for approximately 30 min and would not drop below −20°C for the rest of the expedition. Over the following 5 weeks, multiple warm events pushed the surface toward the melting point, but consistent melt was not reached until May 25, 2020, coincident with an abrupt warming of 5°C. Thereafter, $T_{skin}$ typically remained close to 0°C for the melt season and melt pond development significantly modified the surface (Webster et al., 2022). During June, periodic cold events with $T_{skin}$ reaching as cold as −4°C led to intermittent surface refreezing, sometimes allowing fresh snow to accumulate on ponded surfaces (Webster et al., 2022). Through July at the first MOSAiC ice floe and into August at the second, $T_{skin}$ was typically within 1°C of the melting point. The various components of the SEB are intimately linked with this annual evolution of $T_{skin}$ (e.g., Sledd et al., 2025).

The general principles of the surface LW radiative balance and its relation to atmospheric variability were discussed in Section 3. When viewed over the annual cycle, LWN (**Figures 4a**, S5a, S5b) varied between strong

negative and weak negative values primarily on synoptic time scales that control cloudiness (5–10 days). Time series of cloud occurrence, LWP, and IWP (Figure S4) clearly reveal this variability. As discussed below, variability on similar scales is observed in most energy budget terms, demonstrating the important role of the Arctic atmospheric state. Under mostly clear skies, LWN reached minima of −50 to −60 W $m^{-2}$, which were slightly more negative in April through July due to warmer surface temperatures and weaker temperature inversions. Under the thickest clouds, LWN was closer to 0 W $m^{-2}$, with winter maxima around −10 W $m^{-2}$. Summer maxima were higher, in part because the surface temperature and LW emission of melting sea ice were fixed while the atmosphere was periodically warmer than the surface. Part of this seasonal variation is also related to clouds being more dominated by ice in winter but by optically thicker liquid clouds in the moister and warmer summer (Figures S3, S4). While both the temperature and PWV increased from winter to summer, the moisture increase was more significant, leading to a summer increase in relative humidity, which supported the monthly mean cloud fraction exceeding 85% from May through September. Thus, through most of these months the LWN was more often near 0 W $m^{-2}$ than in its strongly negative state.

Shortwave radiation (**Figures 4a**, S5a, S5c) was not a factor for a significant part of the year, with the polar night at MOSAiC extending from early October to early March. Once present, solar radiation varied on temporal scales similar to LWN and cloudiness. While the daily-average SWD reached nearly 400 W $m^{-2}$ near the summer solstice, the surface SWN only reached a maximum around 100 W $m^{-2}$ due to the high surface albedo (**Figure 4d**). High values of SWN extended well into July, in part due to declining albedo. In spring, prior to surface melt, the albedo varied around 0.8 but started to decline in late May with the onset of snow melt and formation of melt ponds. A brief increase was observed in late June, coincident with a refreeze and snow event (Webster et al., 2022). As the melt season progressed, the albedo declined to a low of about 0.5 in late July before increasing again during the last month of the expedition due to surface freeze and new snow, consistent with Light et al. (2022).

Turbulent heat fluxes (**Figures 4b**, S6a) showed variability that was often related to the impacts of clouds and radiation on the skin temperature (e.g., Persson et al., 2017; Solomon et al., 2023; Sledd et al., 2025), although at times the variability appeared to be stronger and/or unrelated to radiative drivers. $H_l$ was typically weak and, on average, neutral through most of the cold season. It became generally positive in May and June, as the surface lost energy through evaporation when the near-surface RH was not yet saturated, thereafter returning to mostly weakly positive values through the end of the expedition. $H_s$ varied by about an order of magnitude more than $H_l$ in winter, but monthly average values were still quite weak and of the same order of magnitude as $H_l$. On average, $H_s$ was near 0 W $m^{-2}$ in winter, with periodic positive episodes related to passing cyclones balancing frequent surface heating under surface-based temperature inversions. It transitioned to weakly positive in May and June as the near-surface temperature gradient (Figure S3b) diminished along with increasing cloudiness. $H_s$ was again small or weakly negative in July when the surface temperature was fixed at the melting point while atmospheric advection was sometimes warmer than the surface. Additionally, there was a period of significantly positive $H_s$ values in March that are discussed in Section 4.2.

Conduction of heat through the sea ice (**Figures 4c**, S6c) was generally positive (upward) through winter, representing the transfer of heat from the warm ocean below up to the cold surface. Its magnitude varied with $T_{skin}$ in response to atmospheric variability. As the surface started to warm in March, diminishing the temperature gradient through the ice, $C$ also diminished. In summer, $C$ became small as the system was in a state of melt, with a slight reversal of sign because of the vertical gradient in melting point between the fresh surface (0°C) and salty ice bottom (−1.8°C). Lei et al. (2022) showed a similar seasonal cycle of $C$ at MOSAiC, although at coarser temporal resolution.

The total atmospheric heat flux ($F_{atm}$) was significantly driven by $Q_{net}$, which was much larger than the net turbulent heat flux in all months except May, when $Q_{net}$ transitioned from negative to positive with competing SW and LW effects while $H_s$ and $H_l$ were near their annual maxima. $Q_{net}$ and $F_{atm}$ both turned positive briefly during the mid-April warm air intrusion event, supported also by downward $H_s$. This event was followed by multiple late April and early May events when $Q_{net}$ intermittently turned positive but $F_{atm}$ did not always follow suit because of the damping effect of turbulent heat fluxes. From a daily-average perspective, $Q_{net}$ turned consistently positive on May 5 while $F_{atm}$ did not do so consistently until May 13. During the heart of summer, $Q_{net}$ reached maximum values of 75–100 W $m^{-2}$ before again seasonally declining. MOSAiC's fall deployment observed the transition toward negative values at a different ice floe that was much further to the north. In this case, and opposite to the spring transition, $F_{atm}$ reached negative values earlier than $Q_{net}$, with both turning consistently negative in the first couple days of September.

The net surface energy budget ($F_{sfc}$) represents the interplay between $F_{atm}$ and $C$ (**Figures 4c**, S6), with imbalances leading to changes in the surface layer temperature or melt. Since the magnitude of $F_{atm}$ was generally larger than $C$ in winter, $F_{sfc}$ was typically negative and the surface lost energy (**Figures 4c**, S6c). Only during particularly thick cloudy conditions, with diminished surface radiative cooling, did $C$ provide enough heat to overcome the negative $F_{atm}$, leading to a warming of the surface interface. For much of March into early April, $F_{sfc}$ was markedly more negative due to the most extreme positive $H_s$ values of the year, possibly due in part to leads (discussed in Section 4.2).

Following $F_{atm}$, $F_{sfc}$ became positive during the mid-April warm air intrusion event with greatly diminished $C$ and then varied near 0 W $m^{-2}$ for the following 4 weeks. This was a period with little ice growth, but melt had not yet started (i.e., Lei et al., 2022). $F_{sfc}$ turned consistently

positive just before $F_{atm}$ on May 12, aided by the still weakly upward $C$ at the time. Shortly after this period, with increasing $F_{sfc}$, the near-surface $C$ reversed itself and combined with the still upward $C$ in the lower ice to warm the remaining cold core of the sea ice to its melting point during June (Lei et al., 2022). Additionally, by May 25 the surface reached its melting point (**Figure 4d**; as defined following Person, 2012), and the increase in $F_{sfc}$ at the time contributed to snow melt through late June and ice melt thereafter. Peak $F_{sfc}$ reached 100 W m$^{-2}$ in late July. At the second MOSAiC ice floe, $F_{sfc}$ exhibited a brief positive period at the end of August, followed by consistent negative values associated with a system losing energy to the atmosphere through both radiation and turbulence during the start of freeze-up.

This annual depiction of the SEB is broadly consistent with the few existing past SEB measurements over sea ice. At SHEBA (Persson et al., 2002), $F_{sfc}$ was similar to MOSAiC, ranging from −20 to 0 W m$^{-2}$ in winter, transitioning to consistently positive values in early May, and peaking near 100 W m$^{-2}$ in summer. The primary differences at SHEBA were winter $C$ that was about half that of MOSAiC, likely due to thicker ice and snow, and significantly lower peak positive values of $H_s$ during winter cloudy conditions. ASCOS measurements (Sedlar et al., 2011) were coincident with the August–September period of MOSAiC, also showing weak positive $H_s$ and $H_l$, a shift of $C$ from negative back to positive, and the same transition of $Q_{net}$ from positive to negative at the beginning of September. N-ICE occurred during four different drifts covering parts of January through June (Walden et al., 2017). It showed similar variability of $H_s$, although with generally smaller upward values in May and June than at MOSAiC. N-ICE experienced many winter warm air intrusions with peak $T_{skin}$ values warmer than −5°C, significantly warmer than those observed at MOSAiC, which was much farther north during winter, and SHEBA. Finally, $Q_{net}$ at N-ICE turned positive about 1 week after MOSAiC.

### 4.2. EC versus bulk turbulent heat fluxes

Turbulent heat fluxes can be derived using EC or bulk approaches. EC estimates are considered most accurate because they represent direct measurements of the covariance of turbulent motions and changes in temperature (sensible) or moisture (latent). However, sonic anemometer measurements of turbulent winds and fast water vapor measurements can be difficult to implement because of numerous potential uncertainties (Cox et al., 2023e) and high sensitivity to icing on sensor heads, leading to measurement outages. Thus, bulk approaches based on Monin–Obukhov similarity theory that rely on simpler meteorological measurements are often used to ensure temporal consistency and continuity. However, such approaches assume information about, for example, surface roughness length to determine the relevant turbulent exchange coefficients. To capture the average bulk interactions, fixed values for related parameters are typically used, which may not represent the conditions at any specific time and fail to represent temporal surface evolution. Additionally, the nature of the sampled domain can differ between these approaches based on the measurement perspective. EC measurements made at 4–10 m above the surface are influenced by a footprint that can extend hundreds of meters upwind of the measurement location, which may not represent the smaller, local area captured by some other energy budget measurements. The bulk approach relies on measurements at multiple heights, which may represent different spatial footprints. While a full assessment of the bulk versus EC approaches is beyond the scope of this study, we examine the implications of one approach versus the other in terms of the impact on the estimated SEB.

A period from March into early April, which experienced frequent lead activity during MOSAiC (see Supplement Text T3, Figure S7), is used to illustrate differences between the approaches. Time series of EC and bulk $H_s$ are compared in **Figure 5a**, with supporting parameters in the rest of **Figure 5**. For illustration purposes, the original bulk $H_s$ data (Cox et al., 2023e) have also been adjusted to remove a wind-dependent bias relative to the EC approach (see Supplement Text T3). The adjusted bulk $H_s$ shows good agreement with the EC $H_s$ at the beginning and end of the example case and periodically throughout.

Significant divergence between the bulk and EC perspectives, by up to a factor of 6 even after the wind adjustment, occurred when there was local lead activity within a few hundred meters of the measurement site (gray shading in **Figure 5**). While this often resulted in an EC $H_s$ that was significantly more positive (upward) than bulk, it sometimes caused the opposite. The sign of these differences may be related to the vertical location of warm plumes emanating from leads relative to the specific tower instruments used for the two different approaches. For example, the plume could have direct interactions with the 10-m instrumentation but limited effect on the near-surface measurements that play a role in the bulk calculations. Overall, during this 35-day case, the EC $H_s$ was, on average, 11 W m$^{-2}$ greater than the original bulk $H_s$, equivalent to 27 MJ m$^{-2}$ of total additional surface cooling.

These comparisons illustrate the importance of considering how the turbulent heat fluxes are derived. The original bulk $H_s$ for MOSAiC (Cox et al., 2023e), derived using a mean surface roughness length from SHEBA, was generally negative in winter with infrequent positive values (not shown). This bulk approach portrays a very stable Arctic system under persistent low-level temperature inversions, not unlike the results from SHEBA (Persson et al., 2002). A deeper look at MOSAiC EC results suggests that the bulk approach underestimates upward $H_s$. The wind-based adjustment applied here for illustration purposes leads to significantly less negative $H_s$, reveals a much less stable near-surface environment (e.g., Jozef et al. 2023), and may help to inform improved bulk approaches. However, beyond this bias offset, there are other differences between the approaches related to how the measurement systems interact with the physics of the atmosphere. The spatial footprint of individual measurements can be a factor leading to inconsistencies among perspectives. Leads are a feature of the sea ice

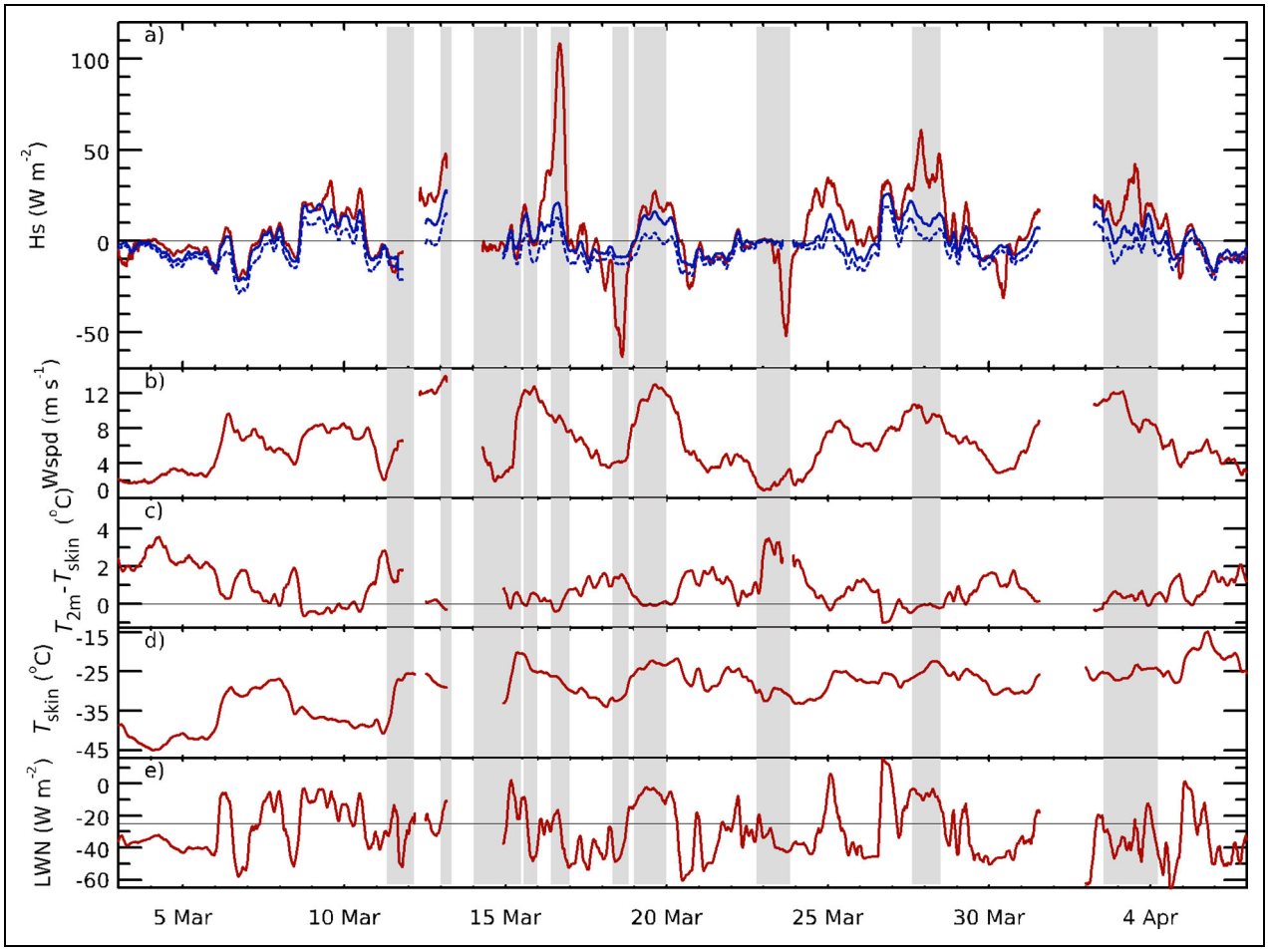


**Figure 5. Example case highlighting differences in sensible heat flux estimates.** A March-to-April time series of 3-h running average (a) eddy covariance (red), original bulk (dashed blue), and adjusted bulk (solid blue) sensible heat flux ($H_s$), (b) 10-m wind speed ($W_{spd}$), (c) near-surface temperature gradient ($T_{2\ m} - T_{skin}$), (d) skin temperature ($T_{skin}$), and (e) net longwave radiation (LWN) from the Met City site. Periods with local lead activity in view of a *Polarstern*-based camera pointed toward Met City are highlighted in gray, although no attempt has been made to determine to what extent these leads are upwind of the measurement site at any given time.

environment and are thus part of the overall heat transfer. However, the rest of our SEB measurements do not sufficiently account for the spatial variability in surface type or related variability in energy transfer that may be captured by the EC $H_s$ under the influence of leads. For example, LWU or $C$ measurements do not represent open leads at all. Thus, while it is important to consider both perspectives on $H_s$, it is also important to note that these differences will naturally lead to imbalances in the full SEB.

## 5. Impact of clouds on the SEB and surface

### *5.1. Atmospheric state effect*

Given this comprehensive quantification of the SEB, we return to the "atmospheric state effect" ($E$) introduced in Section 3.2 and thereby distinguish the contributions from OP and ST atmospheric states. The maximum and net atmospheric state effects (Equations 7 and 8) on the surface are given in **Figure 6**. The average, contributing fluxes for each state to $E$ of many parameters are given in Figures S8–S11, along with state-dependent values for related atmosphere and cloud properties. As context, the ST state is more frequent from December through April, while the OP state is more frequent in May through November (**Figure 6a**). This annual cycle of cloudiness is consistent with the spring increase in liquid-containing clouds observed across the Arctic (e.g., Shupe, 2011; Cesana et al., 2012).

From a radiative standpoint, clouds play the well-established roles of warming the surface in the LW and cooling the surface in the SW. At MOSAiC, the maximum winter LW warming due to the OP state was about 35 W $m^{-2}$, increasing to nearly 60 W $m^{-2}$ in summer (**Figure 6b**). This increase was due to both a summer decrease in LWN during ST conditions due to the weakened vertical temperature gradient and an increase in LWN during OP conditions due to a significantly increased atmospheric opacity (from more liquid water) and periodic temperature inversions over a fixed summer skin temperature (Figures S8b, S9b, S10b). The SW cooling effect of the OP state became increasingly negative as summer evolved reaching a maximum cooling near −60 W $m^{-2}$ in late July, before diminishing to near zero by the end of August. When combined, the cloudy OP state had a net radiative warming effect on the surface throughout the

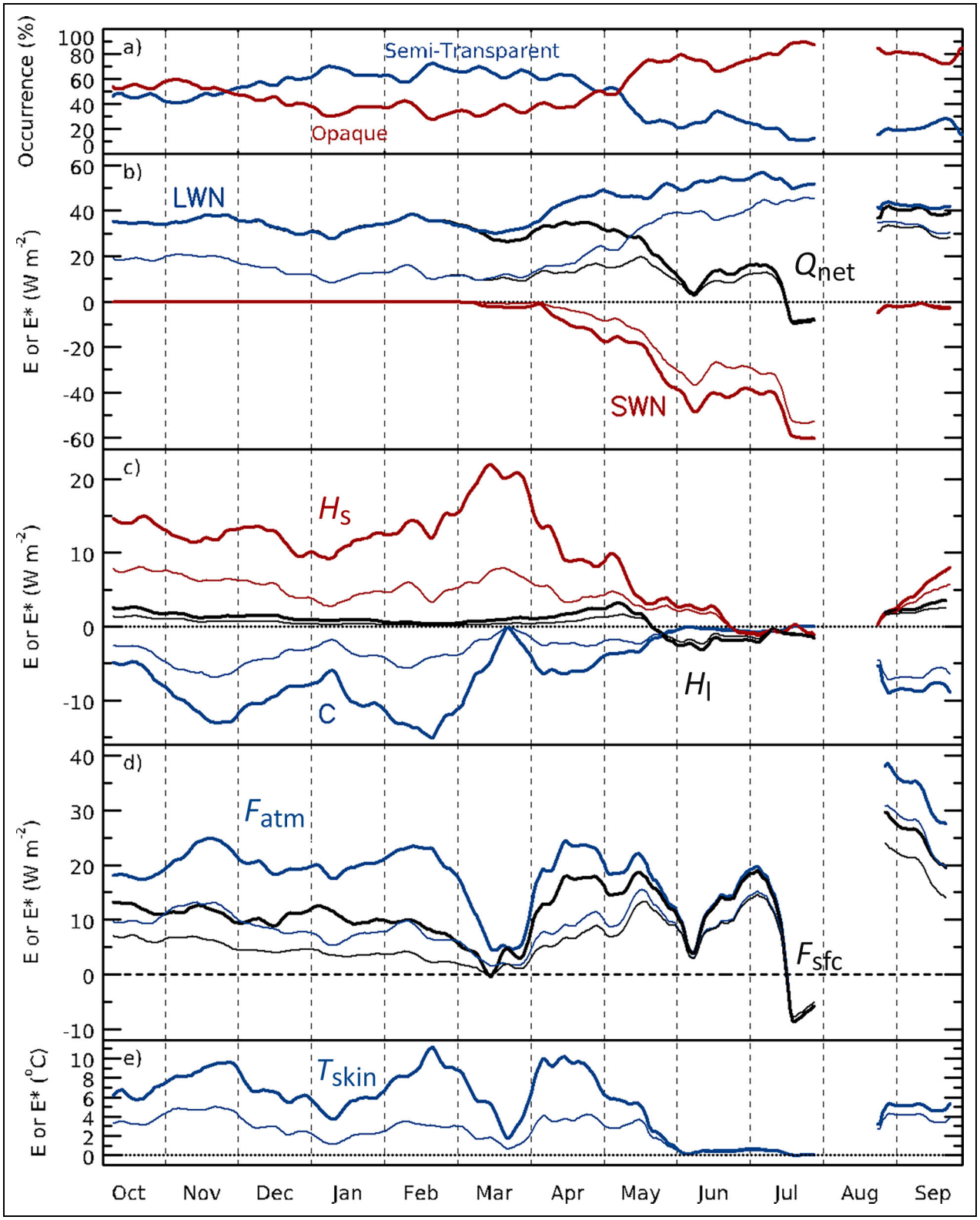


**Figure 6. Atmospheric state effect on surface energy budget parameters.** Maximum ($E$, thick) and net ($E^*$, thin) atmospheric state effect of the opaque state on various surface energy budget terms, including (a) the occurrence fraction of the opaque (OP, red) and semi-transparent (ST, blue) atmospheric states; (b) net longwave (LWN, blue), net shortwave (SWN, red), and net total radiation ($Q_{net}$, black); (c) sensible ($H_s$, red), latent ($H_l$, black), and conductive ($C$, blue) heat fluxes; (d) net atmospheric heat flux ($F_{atm}$, blue) and total surface energy budget ($F_{sfc}$, black); and (e) surface skin temperature ($T_{skin}$). Values are based on the difference in each parameter between the OP and ST states over 30-day running windows ($E$) as given in Figures S8–S11, or this same value scaled by the occurrence fraction for the OP state ($E^*$) as given in panel (a).

whole year except during the second half of July when shortwave cooling became dominant. When taking the occurrence of the OP state into consideration, the net effects ($E^*$) for all terms are decreased in magnitude, most significantly in winter. Compared to past estimates of cloud radiative forcing over sea ice computed in other ways (Intrieri et al., 2002; Stapf et al., 2021; Barrientos-Velasco et al., 2025), these results capture similar general features although naturally reveal some key differences in magnitude as they account for the full impact of the atmospheric state variations.

A rapid shift in the SWN cooling effect in early June before a return to the previous trend is related to an interesting period. Snow melt started on May 25 with an associated decrease in surface albedo (**Figures 4d**, S5d, S10f). After the initial decrease, the albedo stabilized, with $T_{skin}$ 1–2°C below the melting point. On June 7, as a result of snowfall, the albedo increased by nearly 0.1 during an OP state. With this event, $T_{skin}$ also increased up to the melting point, which led to the albedo eventually diminishing again. A couple days later, the ST state occurred under lower albedo conditions. A similar process appears to have occurred again in the following days. The relatively lower average albedo during the ST conditions over this period led to relatively higher SWN than there would have been with a steady albedo, and thus more relative cooling of the surface during contemporaneous OP conditions. This pushed the radiative effect of the OP state briefly toward 0, earlier than it would have otherwise based on typical solar geometry. The system rebounded back to its previous slow decrease of $Q_{net}$, until it went fully negative in the middle of July.

Before examining the other energy transfer terms, it is useful to consider $E(T_{skin})$. Due to surface radiative warming, $T_{skin}$ was warmer by up to 10°C during the OP state in winter compared to ST. This difference is somewhat less than the typical OP state warming observed during N-ICE (Graham et al., 2017). The warming effect diminished in late May as surface melt commenced, fixing the skin at the melting point and making it insensitive to atmospheric state variation. $E(T_{skin})$ again increased into the fall freeze-up period. While some variability in $E(T_{skin})$ might be expected due to interactions among different terms, its marked reduction in late March is a result of an interesting transition. A particularly warm OP event occurred in late February followed by generally colder OP periods, such that the average $T_{skin}$ over the 30-day running window for the OP state decreased through about March 22. Just following the February warm period was an extremely cold ST state followed by substantially warmer ST states, which led to a substantial increase in the 30-day running average $T_{skin}$ more than a week before such an increase for the OP state, bringing the two very close to each other.

In winter both $E(H_s)$ and $E(H_l)$ were positive (**Figure 6c**), representing a surface cooling when the OP state occurred. $E(H_s)$ reached maxima around 15–20 W m$^{-2}$ while $E(H_l)$ was typically less than a couple W m$^{-2}$. These values indicate that in the OP state, the near-surface temperature gradient was diminished relative to the ST state (Figure S8b) and there was slightly more evaporation because the effect of warmer temperature outweighed the effect of more moisture (Figures S8a, S8d). If the bulk approach was used for deriving $E(H_s)$, it diminished somewhat in October and significantly in March, such that the overall winter value was quite steady at approximately 12 W m$^{-2}$ (not shown). In May, $E(H_s)$ diminished significantly until reaching approximately 0 W m$^{-2}$ in late June as $T_{skin}$ became fixed at the melting point, and the near-surface temperature structure became less influenced by the atmospheric state. As $T_{skin}$ cooled into September, the $E(H_s)$ surface cooling effect again reappeared. For $E(H_l)$, the May transition represented a change in sign. In summer, the OP state led to enhanced surface condensation relative to the ST state as the difference in near-surface temperature between states diminished but the difference in near-surface moisture remained (Figure S8). These atmospheric state effects for turbulent heat fluxes are similar in magnitude and variability to those from SHEBA (Intrieri et al., 2002), with seasonal differences in extreme values suggesting variable influence of specific events on each dataset.

$E(C)$ (**Figure 6c**) also underwent a significant annual cycle with some features that mirror other variables. Most important in this regard is $T_{skin}$, which effectively set the temperature gradient through the ice down to the approximately fixed ocean temperature in equilibrium with the ice bottom (−1.8°C). When the OP state occurred, $T_{skin}$ warmed, diminishing the through-ice gradient and decreasing the upward $C$ by 10 ± 5 W m$^{-2}$ in winter. As with other terms dependent on $T_{skin}$, $E(C)$ diminished during the summer melt season before becoming again negative during the freeze-up.

The atmospheric state effect on the net atmospheric flux and net SEB (**Figure 6d**) shows some related features. In winter, $E(F_{atm})$ generally remained around 20 W m$^{-2}$, indicating that the OP state surface cooling effects on $C$ and $H_s$ did not fully compensate for the LW warming. Over this same period, $E(F_{sfc})$ showed a smaller warming than $E(F_{atm})$ because of the compensating cooling effect of $C$. The primary departure from the warming effect of the OP state on these two terms was in March during the period when $H_s$ variability may have been influenced by leads. During this time, the EC $H_s$ tended to have large positive peaks during OP conditions and large negative periods during ST conditions. If the bulk $H_s$ is considered, the March dips in both $E(F_{atm})$ and $E(F_{sfc})$ are diminished significantly. Following the important May transition, the atmospheric state effect on turbulent and conductive heat fluxes diminished such that $E(F_{atm})$ and $E(F_{sfc})$ converged and were primarily driven by radiation. Thus, the early June SW event was also apparent in both terms, as was the transition to a net cooling effect in the second half of July. Following the late summer gap in observations, the OP effects on $F_{atm}$ and $F_{sfc}$ were at their annual maxima because the LW warming effect was still seasonally high, while the SW cooling diminished to 0, in part due to relocation of the observations further north, and the cooling effects of the turbulent heat fluxes had only started to increase.

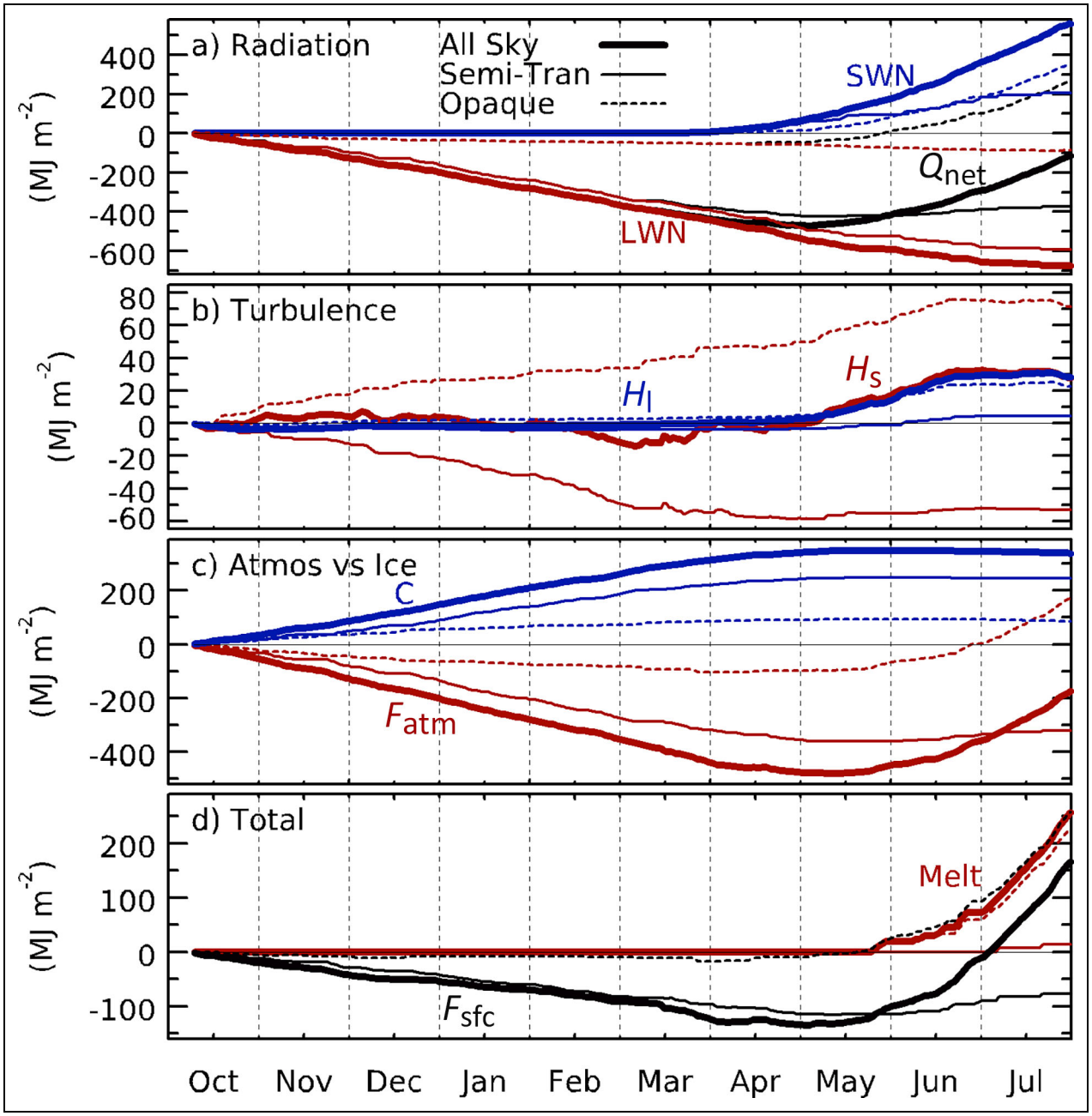


**Figure 7. Cumulative perspective on surface energy budget terms.** Cumulative energy fluxes for (a) net longwave (LWN, red), net shortwave (SWN, blue), and total net radiation ($Q_{net}$, black); (b) sensible ($H_s$, red) and latent ($H_l$, blue) heat fluxes; (c) net atmosphere ($F_{atm}$, red) and conductive ($C$, blue) heat fluxes; and (d) the total surface energy flux ($F_{sfc}$, black) and the excess energy available for melt (red) from the total surface energy flux only at times when the skin temperature is greater than −0.5°C. In each panel, the thick solid curve is the total, while the thin solid curve is for the semi-transparent state and the dashed curve is for the opaque state.

### *5.2. Cumulative SEB*

To understand the temporal evolution of the sea ice energy budget, it is informative to consider a cumulative perspective. Here, we introduce the cumulative energy fluxes for the first MOSAiC ice floe, which drifted from 85°N, 130°E to 79°N, 4°W from October 10, 2019, through July 31, 2020 (**Figure 7**). The August–September part of the expedition was relocated to a different ice floe, such that cumulative fluxes across these two time periods do not represent the same region of ice. Consistent with the atmospheric state analysis, the contributions to cumulative fluxes from both atmospheric states are distinguished to reveal the key roles played by each in the energetic evolution of the system.

LWN radiation is the primary means through which the surface loses energy, promoting upward heat conduction and permitting ice bottom growth. That energy loss at MOSAiC was dominated by the ST state. Over the full 9.5-month period the surface lost 6 times as much LW energy during the ST state compared to the OP state. For SWN, initially the ST state contributed more warming, due to the relatively more frequent occurrence of that state in

the early sunlit season. However, as the summer progressed and the fractional occurrence of the OP state increased, its contribution to the overall solar heating of the surface surpassed the ST state, despite cloud shading effects. $Q_{net}$ followed LWN until the end of March when the SW heating approximately offset the LW cooling for most of April, as the sea ice stopped growing, before overwhelming it through the rest of summer. During summer, the cumulative $Q_{net}$ during ST conditions only slightly increased as the SW warming slightly outweighed the LW cooling in this state. For the OP state, the cumulative $Q_{net}$ increased from May onward and went net positive in late May. Together, the full system showed an overall net radiative cooling of approximately 100 MJ $m^{-2}$ by the end of the period, with a net warming of nearly 300 MJ $m^{-2}$ in the OP state not fully compensating the nearly 400 MJ $m^{-2}$ of cooling during the ST state. Had the time series been longer at the initial MOSAiC ice flow, we speculate that the total cumulative radiative flux would have shifted toward a net warming by mid-August before eventually trending back toward 0 MJ $m^{-2}$ as the solar contribution waned.

The cumulative turbulent heat fluxes showed an interesting story (**Figure 7b**). $H_s$ was much more strongly dependent on the atmospheric state, largely responding to radiative impacts on the near-surface structure, with persistent surface cooling (positive) under the OP state and warming (negative) under the ST state. Through most of the winter until the end of April, these processes approximately offset each other leading to no net accumulated sensible heat. From May through the rest of the time series, there was little net change during the ST state, but $H_s$ continued to cool the surface up to 30 MJ $m^{-2}$ by mid-June during the increasingly frequent OP state. Thereafter, accumulated $H_s$ did not change. $H_l$ was generally small through most of the year (**Figure 4b**) with a weak sensitivity to the atmospheric state. In May and June, there was some net cooling by $H_l$, primarily due to surface evaporation during frequent summer OP conditions, even though evaporative cooling was more efficient during drier ST conditions. The striking finding is that the cumulative $H_s$ and $H_l$ were approximately the same magnitude by the end of July, despite taking markedly different courses to arrive there. However, if the bulk approach is used to derive these heat fluxes the story is quite different. In that case, $H_s$ reached $-110$ MJ $m^{-2}$ by mid-May and remain within about 10 MJ $m^{-2}$ of that value until the end of the period (not shown). Again, this bulk perspective suggests a much more stably stratified lower atmosphere than is portrayed by the EC approach, with dramatically more turbulent surface warming.

Adding the contributions from radiation and turbulence, we see that the cumulative atmospheric heat flux was strongly negative through mid-May, driven primarily by the ST state, while the OP state only contributed about 20% of the net cooling of nearly 500 MJ $m^{-2}$ over this time period. In mid-May, the ST cooling slowed and then started to slightly warm, while the OP state shifted toward significant warming driven by solar radiation. The total cumulative atmospheric heat flux started increasing at this time, ending the period at a net loss of 180 MJ $m^{-2}$, contributed mostly by radiation but also significantly by the total turbulent heat flux. This atmospheric loss, when balanced against the net flux between the ocean and sea ice, determines the overall change in ice thickness (see Section 6).

The surface cumulative $C$ increased through winter, about 3 times as much during ST compared to OP conditions due to colder $T_{skin}$ and a stronger temperature gradient through the sea ice at those times. This warming turned to mostly neutral for both states by May, with weak surface cooling thereafter as the temperature gradient through the ice inverted. The net surface conductive warming of 320 MJ $m^{-2}$ was about 70% during the ST state.

Weighing the cumulative $F_{atm}$ against $C$, we see the evolution of the cumulative total SEB. Its steady negative trend over winter was driven largely by the ST state and surface LW radiative cooling, which made the total surface atmospheric cooling larger than conductive warming over this period. While both the cumulative $F_{atm}$ and $C$ reversed their trends after May, the change in $F_{atm}$ was much stronger, leading to an increasing trend in the net cumulative $F_{sfc}$ after mid-May. This shift was largely driven by SW warming under frequent, summer OP conditions, despite those OP conditions limiting the maximum potential SW warming. By the end of the 9.5-month period, the total cumulative $F_{sfc}$ was positive ($\sim 160$ MJ $m^{-2}$). While this is a net positive value, it does not represent the full sea ice energy budget, which will be discussed in Section 6.

Considering just the periods when the surface temperature was at its melting point ($T_{skin} > -0.5°C$), the cumulative $F_{sfc}$, which is very close to the cumulative $F_{atm}$ over this time, represents the atmospheric contribution to the "energy available for melt." This quantity is equivalent to all the atmospheric energy that goes below the top surface of the snow or sea ice and includes the small amount of solar energy transmitted all the way into the ocean that indirectly impacts the ocean heat flux to the ice. This atmospheric energy for melt started to increase on May 25 at melt onset and increased to about 250 MJ $m^{-2}$ by the end of July (about 50 MJ $m^{-2}$ of this was transmitted to the ocean below the ice).

## 6. SEB and sea ice evolution

The SEB and cloud state analyses provide a detailed accounting of how and why the atmospheric energy available to the sea ice changed over the course of the MOSAiC expedition. One means for evaluating the quality of this analysis is to examine the consistency and closure between the sea ice energy and mass budgets. Here we again focus only on the continuous period from October through July.

Ice growth and snow/ice melt are related to the total energy divergence or convergence, respectively, in the full snow/ice layer. Namely,

$$\Delta D_i + \Delta D_s \rho_s / \rho_i = (-1.0) \times (F_{atm} + F_{ocn} - T_r - \Delta U) \,/\, (L_f \rho_i), \quad (9)$$

where $D_i$ is the ice thickness, $D_s$ is the snow thickness, $F_{atm}$ is the net atmospheric heat flux, $F_{ocn}$ is the ocean heat flux, $T_r$ is the solar energy transmitted through the ice to the ocean, $\rho_s$ is the snow density (300 kg m$^{-3}$), $\rho_i$ is the ice density (900 kg m$^{-3}$), $L_f$ is the latent heat of freezing (0.335 MJ kg$^{-1}$), $\Delta$ represents a change in the given parameter, and $U$ is the storage or internal energy of the sea ice, which is computed as a bulk approximation by analogy to the cold content (CC) equation at any given time as

$$\mathrm{CC} = c_i \rho_i (D_i + D_s \rho_s / \rho_i)(T_{skin} + T_{ocn})/2, \qquad (10)$$

where $T_{ocn}$ is the temperature at the ocean-ice interface ($-1.8$°C) and $c_i$ is the specific heat of ice (0.0021 MJ kg$^{-1}$ °C$^{-1}$). CC represents the instantaneous bulk energy content of the column relative to 0°C, and $\Delta \mathrm{CC} = \Delta U$ (e.g., Jennings et al., 2018). For both equations, snow depth is scaled to equivalent ice thickness by the ratio of snow and ice densities. Increases in snow depth during the accumulation season are not considered in the budget, which can lead to a small imbalance during snowfall. Equation 10 is a simplification of internal energy that inherently assumes a linear temperature profile from the bottom to the top of the ice or snow. In reality, variability of ice temperature in response to atmospheric variability decreases with depth, such that $\Delta U$ will be exaggerated by Equation 10. However, when averaged over long timescales (many weeks) or accumulated over time, Equation 10 is a reasonable approximation. For the cumulative perspective, the CC at time zero is subtracted from the CC time series.

As will be shown, the most significant term on the right-hand side of Equation 9 is $F_{atm}$, which, along with $U$ and to some degree $T_r$, is directly derived from our measurements. To conduct the mass balance closure, the other terms must be approximated from observations reported by others. All relevant terms are shown in **Figure 8**.

The evolution of sea ice thickness and snow depth was measured in multiple ways during MOSAiC including ice mass balance buoys (Lei et al., 2022; Perovich et al., 2023), thickness stake fields (Raphael et al., 2024), and repeated spatial transects using an electromagnetic induction device for total thickness and a Magnaprobe for the snow depth (Itkin et al., 2023). Each perspective measured a different set of ice and snow conditions, with a wide range of ice thicknesses depending on ice age and deformation, and snow depths depending on redistribution around surface features. Here we distill this variable observational information in a way that is most representative of our energy budget observation locations, which were generally on level, second-year sea ice.

For the evolution of ice thickness (**Figure 8c**), Raphael et al. (2024) noted a median thickness of 0.66 m across many stakes installed in October on undeformed second-year ice. A couple of weeks later, Lei et al. (2022) measured a wider range of ice thicknesses, encompassing 0.66 m, at a collection of buoys. The first observations from November 1 reported by Itkin et al. (2023) along the southern transect loop, which was primarily focused on level second-year ice, had a mean of about 0.7 m. Thus, we assume a starting ice thickness of 0.66 m. For the total ice growth by the end of the growing season we draw upon multiple perspectives: Raphael et al. (2024) reported an average ice thickness of approximately 1.95 m in early May, Lei et al. (2022) reported a mean ice bottom depth (not accounting for freeboard and snow) of approximately 1.9 m in mid-May, Perovich et al. (2023; 2025) reported a maximum thickness at one buoy of approximately 1.9 m in mid-May, and Itkin et al. (2023) reported a mean ice thickness around 2 m in early May for the southern transect. Given these values, we estimate an average maximum ice thickness of 1.95 m in place from May 12 at the end of growth (Raphael et al., 2024) through June 7 at the start of basal melt (Lei et al., 2022). Consequently, the mean ice growth rate for our representation of these observations is identical to the mean rate for second-year ice of 0.006 m d$^{-1}$ (Raphael et al., 2024). Lei et al. (2022) reported an average melt of equivalent ice thickness of approximately 0.78 m until July 20, 0.07 m of which was the ice equivalent of the snow depth. To get to this point, we use information from Lei et al. (2022) to depict an initial slow loss of ice in June due to weak basal melt while the snow melted above. Sea ice melt accelerated after snow melt ended in late June. In **Figure 8c**, we give a $\pm$0.35 m shading around the approximated mean evolution of the ice thickness to represent much of the variability, consistent with Lei et al. (2022); however, there were certainly regions of ice outside of this thickness range.

For snow (**Figure 8c**), all five observational sources from the previous paragraph indicate a maximum snow depth between approximately 0.25 and 0.3 m. We adopt the average given by Lei et al. (2022) of 0.25 m, who also indicated little snow accumulation across multiple spring months, and an average snow melt out date of June 25. As discussed previously, snow melt onset was May 25. The accumulation of snow is not important here, as only the total depth and period of snow melt factor into the calculations.

Ocean heat flux to the sea ice was small throughout winter, increasing into summer (**Figure 8a**). We adopt the multisite average from Lei et al. (2022), which included both $F_{ocn}$ and $T_r$. This combined parameter was 4 W m$^{-2}$ in mid-October, decreased to 1.5 W m$^{-2}$ in early December, gradually increased to 4.5 W m$^{-2}$ in early May, and then increased more rapidly into June. Perovich et al. (2023) suggest somewhat higher values at one site in June than Lei et al. (2022), so we adopt an average for mid-June of 15 W m$^{-2}$. Thereafter, both studies suggest a substantial increase in $F_{ocn} - T_r$ as the MOSAiC site neared the sea ice edge in July, but no clear summary statistics are provided. Thus, after consulting a summary of many ocean heat flux measurements (Krishfield and Perovich, 2005) we settled on a value of 65 W m$^{-2}$ at the end of July, which is on the high end of their summer observations as expected near the ice edge. There is significant uncertainty in $F_{ocn} - T_r$ at this time as the entire ice floe broke up on July 31. We extracted $F_{ocn}$ from this combined term by adding our derived $T_r$, which was scaled to match Perovich et al. (2025).

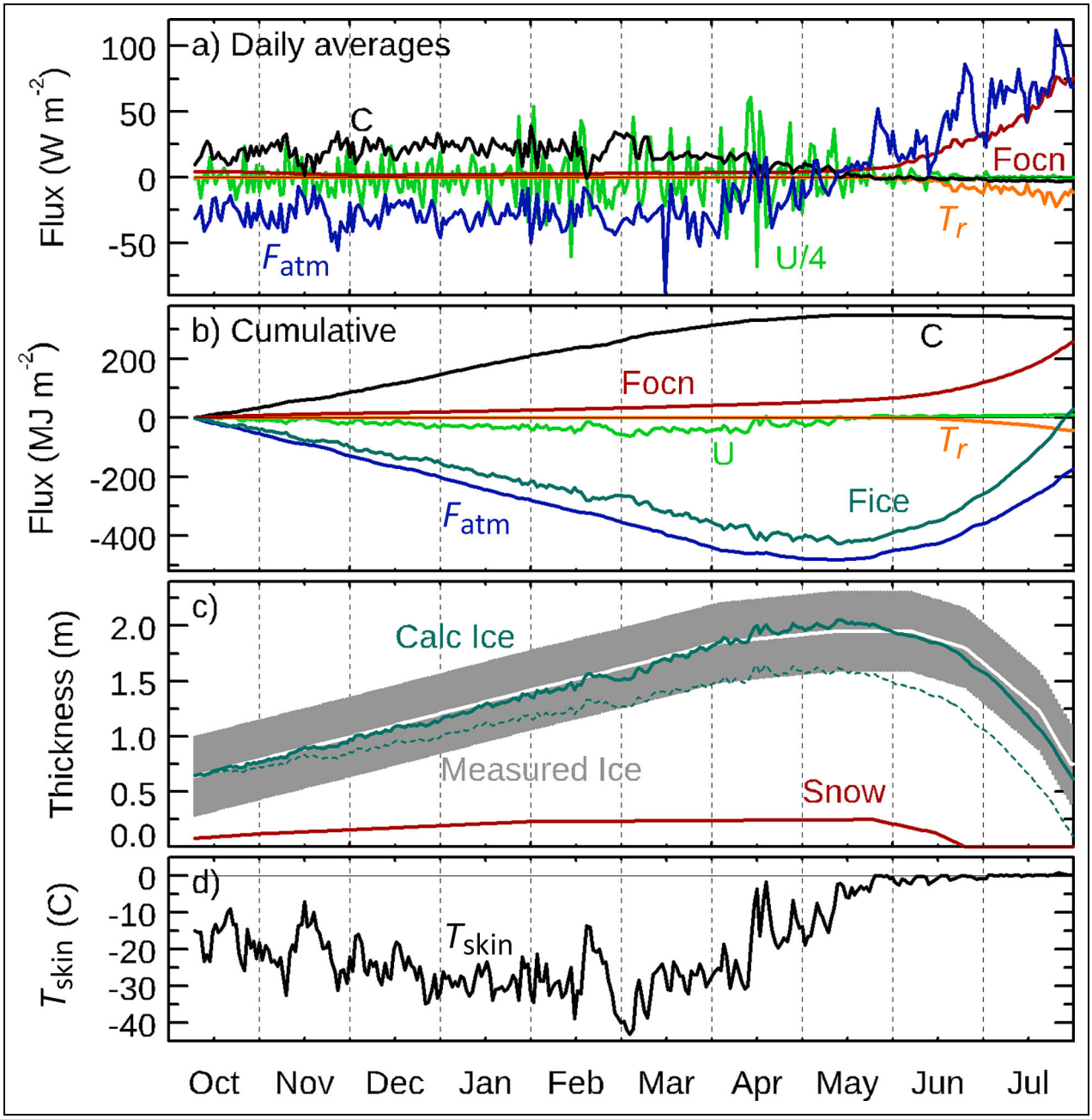


**Figure 8. Assessment of closure between see ice energy and mass budgets.** (a) Time series of the net atmosphere ($F_{atm}$), ocean turbulent ($F_{ocn}$), top of ice conductive ($C$), and fully transmitted solar ($T_r$, multiplied by −1 to express as an energy loss) flux terms along with the flux equivalent to the change in sea ice internal energy ($U$) divided by 4. (b) Cumulative flux contributions for each term, including the total cumulative flux available to change ice thickness and/or melt snow ($F_{ice}$). (c) Observed annual evolution of snow depth (red) and ice thickness (white) along with an approximation of its spatial variability across the MOSAiC domain (gray) all estimated from a collection of independent measurements, plotted along with the sea ice thickness calculated from the flux terms in panels (a) and (b) (solid turquoise). A second estimate of the sea ice thickness using the bulk $H_s$ is also included (dashed turquoise). (d) The measured sea ice skin temperature ($T_{skin}$).

Daily-average fluxes for all key terms are summarized in **Figure 8a**, with cumulative fluxes in **Figure 8b**. The dominant flux during most of the year was $F_{atm}$, which consistently cooled the surface in winter and warmed it after mid-May, ending the full period with a net loss of about 180 MJ m$^{-2}$. $F_{ocn}$ contributed little heat to the sea ice until it started to increase in May, resulting in a net warming over the full period of 250 MJ m$^{-2}$. Variability in sea ice internal energy followed variability of $T_{skin}$ imparted by atmospheric processes. The cumulative $U$ became somewhat negative through winter as the ice cooled but then increased back to slightly positive net values in mid-May and beyond due to net warming and thickening. $T_r$ started to become appreciable in mid-June as the weakly transmissive snow diminished and accounted for 43 MJ m$^{-2}$ of total sea ice heat loss by the

end of July. When combined, the cumulative total energy available for ice growth and snow/ice melt ($F_{ice}$) was dominated by $F_{atm}$ in winter when $F_{ocn}$ and $U$ were small. The difference between $F_{ice}$ and $F_{atm}$ increased through summer as $U$ diminished and $F_{ocn}$ outweighed $T_r$. By the end of July, the cumulative $F_{ice}$ slightly exceeded 0 MJ $m^{-2}$, implying that the ice was slightly thinner than the initial ice thickness in October.

The time series of ice thickness calculated from these fluxes using Equation 9, and initiated at the same starting ice thickness, closely follows the mean ice thickness evolution derived from independent physical observations. While the calculated time series portrays temporal changes in ice growth rate related to atmospheric variability, the mean growth rate over the full growth season is remarkably similar to the observed. The maximum calculated ice thickness is slightly larger than observed, but well within the expected range. The May–June time frame is also not perfectly represented. While there is significant variability and uncertainty in the observed ice melt at this time, the suggestion is that the calculated ice thickness begins to decline too quickly, possibly due to overestimated $F_{ocn}$ or $F_{atm}$ that starts to increase too quickly. Overall, however, the closure between calculated and observed ice thickness is striking.

For comparison, the ice growth and melt cycle was also calculated using the original bulk $H_s$ in $F_{atm}$. Results (**Figure 8c**) show an ice cycle that is vastly different from the observed, with a winter growth rate that is underestimated by about 30%. This comparison suggests that the EC version of $H_s$ is substantially more consistent with the rest of the measurements than the bulk version.

One last aspect of this closure study is to examine the net growth and melt season balances. Here we delineate these by the date of May 13; while snow melt did not start until May 25, the system was in approximate steady state during the intervening period, and May 13 was the time of thickest sea ice. During growth season, the cumulative fluxes of $F_{atm}$ (−481 MJ $m^{-2}$), $F_{ocn}$ (57 MJ $m^{-2}$), $T_r$ (0 MJ $m^{-2}$), and the change in $U$ (3 MJ $m^{-2}$) total −427 MJ $m^{-2}$ that went into ice growth. However, since ice growth occurs only at ice bottom, the cumulative derived $C$ at the surface (347 MJ $m^{-2}$) was approximately 130 MJ $m^{-2}$ too small to move all necessary heat from the ice bottom to the ice/snow top, which was the source of cooling. We do not understand the cause of this 28% deficit as estimated errors in the temperature gradient through the ice/snow or the assumed thermal conductivities of ice and/or snow are not large enough to make up the difference. Some contribution may be related to the $H_s$, which was at times influenced by vertical heat transfer through leads that was not consistent with other measurements.

When considering the melt season from May 13 through July 31, there is a different balance. The cumulative fluxes of $F_{atm}$ (302 MJ $m^{-2}$), $F_{ocn}$ (197 MJ $m^{-2}$), $T_r$ (42 MJ $m^{-2}$), and the change in $U$ (7 MJ $m^{-2}$) totaled 450 MJ $m^{-2}$, of which 25 MJ $m^{-2}$ melted snow and the rest melted sea ice. The cumulative $C$ was −8 MJ $m^{-2}$. By considering the budgets at the sea ice top versus bottom, the top had approximately 66% of the total energy for melt, while the bottom had 34%, in agreement with Lei et al. (2022).

By partitioning the contributions to the ice thickness change calculated using Equation 9 by atmospheric state, and assuming $F_{ocn}$ is independent of atmospheric state, approximately 79% of ice growth happened during the ST state, which occurred for 57% of the growth season. This implies an ice growth rate that is about 2.8 times larger during the ST compared to the OP state due to more intense surface cooling. On the other hand, 90% of the total melt happened during the 77% of the time the OP state occurred from May 13 through July 31, implying a melt rate that is about 2.7 times larger during the OP state compared to the ST state due to more net warming under OP conditions (e.g., **Figure 6d**). These comparative rates are approximately proportional to the two states' relative slopes of seasonally cumulative $F_{atm}$ (**Figure 7c**), as the biggest atmospheric contributor to ice thickness change.

## 7. Discussion and conclusions

The SEB is central to an Arctic system in a state of rapid change. Here, we have leveraged a collection of particularly rare measurements over the central Arctic sea ice during the MOSAiC expedition to characterize the annual variability of the SEB and examine how it is impacted by the two dominant radiative states of the Arctic atmosphere.

The bimodal nature of the Arctic atmosphere is distinguished into the ST and OP states based on surface net longwave radiation (e.g., Stramler et al., 2011). This study utilizes a suite of cloud and meteorological observations made on and around *Polarstern* to explore important details that characterize fundamental cloud and atmosphere properties of each state. It was found that over the course of the MOSAiC observational year each state occurred approximately half of the time, with seasonal variation. The ST state occurred more frequently in the long winter, while in May there was a marked transition toward more frequent OP conditions through late fall.

The presence or absence of liquid water is a first-order control on Arctic atmospheric radiation (Shupe and Intrieri, 2004) and thus the atmospheric state. MOSAiC observations reveal that the OP state typically contained cloud liquid water, while the ST state did not. However, ultimately the states are determined by the overall opacity of the atmosphere, which is in principle independent of cloud phase. Indeed, 21% of OP state occurrences did not contain liquid water but instead contained significant cloud ice. This ice generally occurred in larger amounts during the OP state but also occurred during the ST state. Coincident with its cloudier conditions, the OP state often had substantially more PWV, more frequent warm temperatures, and a distribution of near-surface temperature gradient centered near zero (i.e., near neutral). The ST state occurred under primarily stable near-surface stratification, except during mid-summer. Interestingly, there was no strong dependence of atmospheric state on surface pressure. Only in January–April did the less frequent OP state occur under average surface pressure that was at least 5 hPa lower than the ST state. The limited influence of

pressure on atmospheric state may be due to the diversity of circulation patterns in the Atlantic sector of the Arctic, compared to the more static large-scale pressure pattern in the western Arctic.

SEB measurements were made at multiple sites across the MOSAiC domain with a combination of attended and semiautonomous systems. These measurements spanned the full MOSAiC year, apart from a period in August when *Polarstern* was relocated and the instrumentation was temporarily brought onboard. Importantly, a semiautonomous station was able to bridge an earlier gap when *Polarstern* also left the sea ice, enabling essential measurements of the spring melt onset. Due to recent technological advances in many aspects of the measurement system, these data are of high quality relative to past energy budget measurements over sea ice (e.g., Persson et al., 2002). Thus, the derived dataset (Cox et al., 2023e) can reasonably be considered the most comprehensive and high-quality SEB product available for the Arctic sea ice domain. However, the drifting nature of the observations in this "sea ice Lagrangian" perspective must be kept in mind when interpreting the results and should not be confused with an Eulerian perspective from a fixed location in space.

The SEB went from weakly negative during ice growth in winter, turning significantly positive starting on May 12 through the melt season, before returning to negative values by the end of August with the onset of surface freeze. SEB variability was largely driven by radiation but influenced by many processes. Such variability played out on synoptic time scales (days up to 1 week) where atmosphere-driven perturbations to surface radiation led to co-variability in other energy budget terms. Additionally, the seasonal cycle of insolation and the relationship of $T_{skin}$ to the melting point drove significant regime shifts in energy partitioning across the system. Sledd et al. (2025) provide a detailed quantification of the process interactions among SEB terms that played out on synoptic and seasonal time scales.

To explore the influence of atmospheric state on the SEB and other terms, we defined the atmospheric state effect ($E$) to delineate the maximum impact of the OP state on a given parameter relative to the ST state. While in some ways analogous to cloud radiative forcing, this parameter considers all concomitant variability of the atmosphere that includes cloudiness, moisture, and temperature. Importantly, this approach allows for an analysis of the effect on all terms not just radiation. To our knowledge this type of approach has not been previously applied to the complete SEB.

The atmospheric state effect on SEB terms at MOSAiC underwent important seasonal variations that are strongly constrained by the ability of $T_{skin}$ to respond to atmospheric perturbations (non-melt season) or not (melt season). These distinct surface regimes allow us to generalize the atmospheric interactions with the central Arctic sea ice surface during the ice growth versus melt seasons. The following general results neglect sub-seasonal variations that are often the result of specific events. During winter ice growth, the typical $E$(LWN) was approximately 35 W $m^{-2}$ (surface warming), $E(H_s)$ was 15 W $m^{-2}$ (cooling), $E(H_l)$ was 1 W $m^{-2}$ (cooling), and $E(C)$ was $-10$ W $m^{-2}$ (cooling), resulting in a net atmospheric warming effect of 20 W $m^{-2}$, and a net total surface energy flux effect of 10 W $m^{-2}$. $T_{skin}$ was approximately 8°C warmer under OP conditions. At this time of year, the system represented a radiative-turbulent-conductive balance, coupled via $T_{skin}$, which during this season was typically cold and responsive to perturbations. In winter, the fluxes were heightened (larger in magnitude) under the ST state because of stronger stratification and steeper near-surface temperature gradients caused by efficient surface radiative cooling. Nearly all accumulated winter surface cooling occurred during the ST state, with little during the OP state.

With the onset of sunlight in March, the system began a transition toward its summer, melt state. $E$(LWN) became increasingly positive, counteracting the increasingly negative $E$(SWN) as the sun rose higher in the sky and the surface albedo declined. By early May, $Q_{net}$ turned positive and $E(Q_{net})$ started to decrease as the solar effect became dominant, eventually turning net negative during the second half of July as the OP state briefly cooled the surface. During the spring transition, the magnitudes of $H_s$ and $H_l$ both increased, while $C$ decreased, but the atmospheric state effect for all these terms diminished substantially as $T_{skin}$ approached the melting point and became unresponsive to variations in atmospheric state. As a result, $E(F_{atm})$ and $E(F_{sfc})$ converged on $E(Q_{net})$, and the system arrived at a primary balance between radiation and surface melt. Overall, surface warming via SWN drove most summer melt, with most of this net SW warming occurring during the frequent OP state despite its tendency to shade the surface from sunlight relative to the ST state. Thus, while the ST state dominated winter cooling, the OP state dominated summer warming.

One other aspect of the energy budget is particularly interesting. Cumulatively, $H_s$ and $H_l$ had approximately the same net impact of 0 MJ $m^{-2}$ on the surface during the winter growth season and both cooled the surface by approximately 30 MJ $m^{-2}$ during the transition to summer melt. The May increase in both terms resulted from increased positive contributions from the increasingly frequent OP state. However, in winter, while $H_l$ was always small, $H_s$ was highly variable, striking a remarkable cumulative balance between surface warming under strong near-surface stability in the ST state and surface cooling during periodic storms and cloudiness in the OP state. This result contrasts with those from SHEBA (Persson et al., 2002) where negative winter $H_s$ led to a net surface warming of about 75 MJ $m^{-2}$ over the ice growth season. Thus, while the canonical notion from past observations is that the Arctic winter is highly stably stratified, the balance between downward and upward $H_s$ at MOSAiC suggests a softening of that view.

The overall quality of the SEB measurements and derived products was exhibited through surface energy and mass budget closure. While there was a great deal of spatial and temporal variability at MOSAiC, which poses a challenge for closing any budget, the changes in sea ice thickness implied by the SEB measurements matched

remarkably well with independent observations from multiple sources. Observations (Raphael et al., 2024) and calculations nearly identically agree on an average winter ice growth rate of 0.006 m $d^{-1}$. This closure analysis not only demonstrates the consistency and high quality of the measurements but also reveals an important achievement in synthesis across many different measurement systems and programs at MOSAiC. Additionally, the strong seasonally counteracting influences of the OP versus ST states, with ST showing a 2.8 times larger ice growth rate and OP showing a 2.7 times larger ice melt rate, suggest that any significant change in temporal fractionation of these states would have a dramatic impact on the annual evolution of sea ice thickness.

Despite reasonable closure in this case, observational challenges remain when considering the SEB of Arctic sea ice. One challenge involves combining different measurements that represent distinct spatial footprints that may be comprised of variable snow depth and ice thickness, ice structural properties, melt ponds, and open water, each with distinct heat transfer properties. This point was highlighted at MOSAiC by the differences between turbulent heat fluxes derived using the EC approach versus a bulk approach that we believe is the best distillation of past research. When applied to MOSAiC observations, the EC approach provided a substantially more positive average $H_s$ that resulted in excellent closure with the sea ice mass. The bulk approach yielded results that were more similar to SHEBA (Persson et al., 2002) yet did not compare well with the observed variation of ice thickness. A comprehensive study comparing EC and bulk approaches is needed to delineate the differences between the two perspectives and to improve the bulk approach based on this new MOSAiC data.

Overall, the MOSAiC dataset represents an important advance in our understanding of the central Arctic SEB. This high-quality dataset has already been used to evaluate a wide variety of models (Heinemann et al., 2022; Herrmannsdörfer et al., 2023; Pithan et al., 2023; Solomon et al., 2023; Schnierstein et al., 2024; Sledd et al., 2025) and satellite observations (Huang et al., 2022). Yet these observations offer only a singular perspective on the annual cycle at one drifting location in the Arctic sea ice. The question remains how representative these measurements and findings are of the broader Arctic sea ice domain now and into the future. With so few observations of this type, the community needs many more measurements with which to better understand spatial and interseasonal variability, to ascertain how surface heterogeneity impacts energy transfer on the aggregate scales represented in models, and to identify the evolving role of SEB processes in continued Arctic change. To this end, more efforts should be given toward development of autonomous technologies for measuring the SEB with high fidelity in challenging polar environments.

## Appendix A. Parameters, variables, and symbols

$A_c$: cloud occurrence fraction, %

$A_{op}$: fractional occurrence of the opaque atmospheric state, fraction

$C$: conductive heat flux upward at top of sea ice/snow, positive upward, W $m^{-2}$

$C_b$: conductive heat flux upward from bottom of sea ice, positive upward, W $m^{-2}$

CC: cold content, MJ $m^{-2}$

$c_i$: specific heat of ice, assumed to be 0.0021 MJ $kg^{-1}$ $°C^{-1}$

$D_i$: thickness of sea ice, m

$D_s$: depth of snow, m

$E(P)$: maximum atmospheric state effect on parameter $P$, units of $P$

$E^*(P)$: net atmospheric state effect on parameter $P$, units of $P$

$F_{atm}$: net atmospheric heat flux at surface, positive downward, W $m^{-2}$

$F_{bot}$: net energy flux density at the sea ice bottom, positive upward, W $m^{-2}$

$f_n$: weighting for near-infrared portion of transmitted solar flux, assumed to be 0.4

$F_{net}$: net energy budget of sea ice/snow, positive downward, W $m^{-2}$

$F_{ocn}$: ocean to ice turbulent heat flux, positive upward, W $m^{-2}$

$F_{sfc}$: net energy flux density at surface, positive downward, W $m^{-2}$

$f_v$: weighting for visible portion of transmitted solar flux, assumed to be 0.6

$H_l$: surface latent heat flux, positive upward, W $m^{-2}$

$H_s$: surface sensible heat flux, positive upward, W $m^{-2}$

$I_n$: sea ice surface transmission parameter for near-infrared wavelengths, assumed to be 0.37

$I_o$: snow surface transmission parameter for all wavelengths, assumed to be 0.3

IWC: ice water content, g $m^{-3}$

IWP: ice water path, g $m^{-2}$

$I_v$: sea ice surface transmission parameter for visible wavelengths, assumed to be 0.95

$k_i$: thermal conductivity of sea ice, assumed to be 2.0 W $m^{-1}$ $K^{-1}$

$K_{in}$: sea ice extinction coefficient of near-infrared wavelengths, assumed to be 4.6 $m^{-1}$

$K_{iv}$: sea ice extinction coefficient of visible wavelengths, assumed to be 0.72 $m^{-1}$

$K_s$: snow extinction coefficient of all wavelengths, assumed to range from 3 to 16 $m^{-1}$

$k_s$: thermal conductivity of snow, assumed to be 0.4 W $m^{-1}$ $K^{-1}$

$L_f$: latent heat of freezing, assumed to be 0.335 MJ $kg^{-1}$

LWC: liquid water content, g $m^{-3}$

LWD: downwelling longwave radiative flux at the surface, W $m^{-2}$

LWN: net longwave radiative flux at the surface, positive downward, W $m^{-2}$

LWP: liquid water path, g $m^{-2}$

LWU: upwelling longwave radiative flux at the surface, W $m^{-2}$

$M$: mass of the sea ice/snow, kg

OP: opaque state of the atmosphere

$P_{2\ m}$: atmospheric pressure at 2 m height, hPa
$P_{op}$: average value of a parameter $P$ during the opaque atmospheric state, units of $P$
$P_{st}$: average value of a parameter $P$ during the semi-transparent atmospheric state, units of $P$
PWV: precipitable water vapor, kg $m^{-2}$
$Q_{net}$: net radiative flux at surface, positive downward, W $m^{-2}$
$RH_{2\ m}$: relative humidity at 2 m height, %
SEB: surface energy budget, equivalent to $F_{net}$, positive downward, W $m^{-2}$
ST: semi-transparent state of the atmosphere
SWD: downwelling shortwave radiative flux at the surface, W $m^{-2}$
SWN: net shortwave radiative flux at the surface, positive downward, W $m^{-2}$
SWU: upwelling shortwave radiative flux at the surface, W $m^{-2}$
$T_{2\ m}$: atmospheric temperature at 2 m height, °C
$T_{ocn}$: ocean temperature at sea ice bottom, assumed to be −1.8°C
$T_t$: transmitted solar flux, positive downward, W $m^{-2}$
$T_{skin}$: surface skin temperature, °C
TWP: total condensed water path, g $m^{-2}$
$U$: internal energy or storage of the sea ice/snow, MJ $m^{-2}$
$\alpha$: surface broadband albedo, unitless
$\rho_i$: density of sea ice, assumed to be 900 kg $m^{-3}$
$\rho_s$: density of snow, assumed to be 300 kg $m^{-3}$

## Data accessibility statement

Met City and ASFS surface energy budget and meteorological measurements are available from Cox et al. (2023a; 2023b; 2023c; 2023d). Derived winter snow and ice thermal properties are available from Sledd et al. (2023). Cloud occurrence and properties are available from Shupe (2022). Panomax photographs of the sea ice are available from Nicolaus et al. (2021).

## Supplemental files

The supplemental files for this article can be found as follows:

Supplemental Material.docx

## Acknowledgments

Data used in this article were produced as part of the international Multidisciplinary drifting Observatory for the Study of Arctic Climate (MOSAiC) expedition with tag MOSAiC20192020 and Project_ID: AWI_PS122_00. Some data were collected by the Atmospheric Radiation Measurement User Facility, a DOE Office of Science user facility operated by the Biological and Environmental Research program. We thank all people involved in the MOSAiC expedition as listed in Nixdorf et al. (2021). Dr Nils Fuchs provided useful information on snow optical properties. Dr Jen-Wen Bao offered constructive feedback via an internal review. The statements, findings, conclusions, and recommendations are those of the authors and do not necessarily reflect the views of NOAA or the U.S. Department of Commerce.

## Funding

This research was supported by the National Science Foundation (OPP-1724551, OPP-2138785, OPP-1724424, OPP-1724540), NOAA's Physical Sciences Laboratory (via Cooperative Agreement NA22OAR4320151) and Global Ocean Monitoring and Observing Program (FundRef https://doi.org/10.13039/100018302), the DOE Atmospheric System Research Program (DE-SC0021341) and Atmospheric Radiation Measurement Program, and the U.K. Natural Environment Research Council (grant NE/S002472/1). MDS was also supported by a Mercator Fellowship from the Deutsche Forschungsgemeinschaft (DFG)—project number 268020496—within the Transregional Collaborative Research Center TRR 172, "Arctic Amplification: Climate Relevant Atmospheric and Surface Processes and Feedback Mechanisms (AC)[3]."

## Competing interests

All authors declare that they have no competing interests. BB is an associate editor for *Elementa* and MDS is a guest editor for the *Elementa* Special Feature on MOSAiC. Neither were involved in the editorial or review process for this manuscript.

## Author contributions

Contributed to conception and design: MDS, POGP, CJC, MRG, ASo, BB, IMB, DP, TU.
Contributed to acquisition of data: MDS, POGP, CJC, MRG, BB, IMB, DC, JO, DP, TU.
Contributed to analysis and interpretation of data: MDS, POGP, CJC, MRG, ASo, ASl, BB, IMB, DP, LDR.
Drafted and/or revised the article: All authors.
Approved the submitted version for the publication: All authors.

## References

**Andreas, EL**, **Persson, POG**, **Grachev, AA**, **Jordan, RE**, **Horst, TW**, **Guest, PS**, **Fairall, CW.** 2010. Parameterizing turbulent exchange over sea ice in winter. *Journal of Hydrometeorology* **11**: 87–104. DOI: https://doi.org/10.1175/2009JHM1102.1.

**Barrientos-Velasco, C**, **Cox, CJ**, **Deneke, H**, **Dodson, JB**, **Hunerbein, A**, **Shupe, MD**, **Taylor, PC**, **Macke, A.** 2025. Estimation of the radiation budget during MOSAiC based on ground-based and satellite remote sensing observations. *Atmospheric Chemistry and Physics* **25**: 3929–3960. DOI: https://doi.org/10.5194/acp-25-3929-2025.

**Barton, NP**, **Klein, SA**, **Boyle, JS.** 2014. On the contribution of longwave radiation to global climate model biases in Arctic lower tropospheric stability. *Journal of Climate* **27**(19): 7250–7269. DOI: https://doi.org/10.1175/JCLI-D-14-00126.1.

**Bertossa, C**, **L'Ecuyer, T.** 2024. Two ubiquitous radiative states observed across the high latitudes. *Journal of Climate* **37**: 2585–2610. DOI: https://doi.org/10.1175/JCLI-D-23-0553.1.

**Boeke, RC**, **Taylor, PC.** 2016. Evaluation of the Arctic surface radiation budget in CMIP5 models. *Journal of Geophysical Research: Atmospheres* **121**(14): 8525–8548. DOI: https://doi.org/10.1002/2016JD025099.

**Boisvert, LN**, **Markus, T**, **Vihma, T.** 2013. Moisture flux changes and trends for the entire Arctic in 2003–2011 derived from EOS Aqua data. *Journal of Geophysical Research: Oceans* **118**: 5829–5843. DOI: https://doi.org/10.1002/jgrc.20414.

**Bourassa, MA**, **Gille, ST**, **Bitz, C**, **Carlson, D**, **Cerovechi, I**, **Clayson, CA**, **Cronin, MF**, **Drennan, WM**, **Fairall, CW**, **Hoffman, RN**, **Magnusdottir, G**, **Pinker, RT**, **Renfrew, IA**, **Serreze, M**, **Speer, K**, **Talley, LD**, **Wick, GA.** 2013. High-latitude ocean and sea ice surface fluxes: Challenges for climate research. *Bulletin of the American Meteorological Society* **94**(3): 403–423. DOI: https://doi.org/10.1175/BAMS-D-11-00244.1.

**Brooks, IM**, **Tjernström, M**, **Persson, POG**, **Shupe, MD**, **Atkinson, RA**, **Canut, G**, **Birch, CE**, **Mauritsen, T**, **Sedlar, J**, **Brooks, BJ.** 2017. The turbulent structure of the Arctic summer boundary layer during the Arctic Summer Cloud–Ocean Study. *Journal of Geophysical Research: Atmospheres* **122**: 9685–9704. DOI: https://doi.org/10.1002/2017JD027234.

**Cesana, G**, **Kay, JE**, **Chepfer, H**, **English, JM**, **de Boer, G.** 2012. Ubiquitous low-level liquid-containing Arctic clouds: New observations and climate model constraints from CALIPSO-GOCCP. *Geophysical Research Letters* **39**. DOI: https://doi.org/10.1029/2012GL053385.

**Chung, E-S**, **Ha, K-J**, **Timmermann, A**, **Stuecker, MF**, **Bodai, T**, **Lee, S-K.** 2021. Cold-season Arctic amplification driven by Arctic Ocean-mediated seasonal energy transfer. *Earth's Future* **9**(2): e2020EF001898. DOI: https://doi.org/10.1029/2020EF001898.

**Cox, C**, **Gallagher, M**, **Shupe, M**, **Persson, O**, **Blomquist, B**, **Grachev, A**, **Riihimaki, L**, **Kutchenreiter, M**, **Morris, V**, **Solomon, A**, **Brooks, I**, **Costa, D**, **Gottas, D**, **Hutchings, J**, **Osborn, J**, **Morris, S**, **Preusser, A**, **Uttal, T.** 2023a. Met City meteorological and surface flux measurements (Level 3 Final), Multidisciplinary Drifting Observatory for the Study of Arctic Climate (MOSAiC), central Arctic, October 2019–September 2020. Arctic Data Center. DOI: https://doi.org/10.18739/A2PV6B83F.

**Cox, C**, **Gallagher, M**, **Shupe, M**, **Persson, O**, **Grachev, A**, **Solomon, A**, **Ayers, T**, **Costa, D**, **Hutchings, J**, **Leach, J**, **Morris, S**, **Osborn, J**, **Pezoa, S**, **Uttal, T.** 2023b. Atmospheric Surface Flux Station #30 measurements (Level 3 Final), Multidisciplinary Drifting Observatory for the Study of Arctic Climate (MOSAiC), central Arctic, October 2019–September 2020. Arctic Data Center. DOI: https://doi.org/10.18739/A2FF3M18K.

**Cox, C**, **Gallagher, M**, **Shupe, M**, **Persson, O**, **Grachev, A**, **Solomon, A**, **Ayers, T**, **Costa, D**, **Hutchings, J**, **Leach, J**, **Morris, S**, **Osborn, J**, **Pezoa, S**, **Uttal, T.** 2023c. Atmospheric Surface Flux Station #40 measurements (Level 3 Final), Multidisciplinary Drifting Observatory for the Study of Arctic Climate (MOSAiC), central Arctic, October 2019–September 2020. Arctic Data Center. DOI: https://doi.org/10.18739/A25X25F0P.

**Cox, C**, **Gallagher, M**, **Shupe, M**, **Persson, O**, **Grachev, A**, **Solomon, A**, **Ayers, T**, **Costa, D**, **Hutchings, J**, **Leach, J**, **Morris, S**, **Osborn, J**, **Pezoa, S**, **Uttal, T.** 2023d. Atmospheric Surface Flux Station #50 measurements (Level 3 Final), Multidisciplinary Drifting Observatory for the Study of Arctic Climate (MOSAiC), central Arctic, October 2019–September 2020. Arctic Data Center. DOI: https://doi.org/10.18739/A2XD0R00S.

**Cox, CJ**, **Gallagher, MR**, **Shupe, MD**, **Persson, POG**, **Solomon, A**, **Fairall, CW**, **Ayers, T**, **Blomquist, B**, **Brooks, IM**, **Costa, D**, **Grachev, A**, **Gottas, D**, **Hutchings, JK**, **Kutchenreiter, M**, **Leach, J**, **Morris, SM**, **Morris, V**, **Osborn, J**, **Pezoa, S**, **Preußer, A**, **Riihimaki, LD**, **Uttal, T.** 2023e. Continuous observations of the surface energy budget and meteorology over the Arctic sea ice during MOSAiC. *Scientific Data* **10**(1): 519. DOI: https://doi.org/10.1038/s41597-023-02415-5.

**Cox, CJ**, **Walden, VP**, **Rowe, PM.** 2012. A comparison of the atmospheric conditions at Eureka, Canada, and Barrow, Alaska (2006–2008). *Journal of Geophysical Research: Atmospheres* **117**. DOI: https://doi.org/10.1029/2011JD017164.

**Dahlke, S**, **Rinke, A**, **Shupe, MD**, **Cox, CJ.** 2025. The two Arctic wintertime boundary layer states: Disentangling the role of cloud and wind regimes in reanalysis and observations during MOSAiC. *Atmospheric Science Letters* **26**: e1298. DOI: https://doi.org/10.1002/asl.1298.

**Dai, A**, **Song, M.** 2020. Little influence of Arctic amplification on mid-latitude climate. *Nature Climate Change* **10**: 231–237. DOI: https://doi.org/10.1038/s41558-020-0694-3.

**Dong, X**, **Xi, B**, **Crosby, K**, **Long, CN**, **Stone, RS**, **Shupe, MD.** 2010. A 10 year climatology of Arctic cloud fraction and radiative forcing at Barrow, Alaska. *Journal of Geophysical Research: Atmospheres* **115**: D17212. DOI: https://doi.org/10.1029/2009JD013489.

**Duffey, A**, **Mallett, R**, **Dutch, VR**, **Steckling, J**, **Hermant, A**, **Day, J**, **Pithan, F.** 2025. Representation of Arctic winter atmospheric boundary layer stability over sea ice in CMIP6 models. *Journal of Geophysical Research: Atmospheres* **130**(11): e2024JD041412. DOI: https://doi.org/10.1029/2024JD041412.

**Ebell, K**, **Walbröl, A**, **Engelmann, R**, **Griesche, H**, **Radenz, M**, **Hofer, J**, **Althausen, D.** 2022. Temperature and humidity profiles, integrated water vapour and liquid water path derived from the HATPRO microwave radiometer onboard the Polarstern during the MOSAiC expedition [dataset]. PANGAEA. DOI: https://doi.org/10.1594/PANGAEA.941389.

**Engström, A**, **Karlsson, J**, **Svensson, G.** 2014. The importance of representing mixed-phase clouds for simulating distinctive atmospheric states in the Arctic. *Journal of Climate* **27**(1): 265–272. DOI: https://doi.org/10.1175/JCLI-D-13-00271.1.

**Francis, J**, **Vavrus, S.** 2021. How is rapid Arctic warming influencing weather patterns in lower latitudes? *Arctic, Antarctic, and Alpine Research* **53**(1): 219–220. DOI: https://doi.org/10.1080/15230430.2021.1942400.

**Frolov, IE**, **Gudkovich, ZM**, **Radionov, VF**, **Shiroshkov, AV**, **Timokhov, LA.** 2005. *The Arctic Basin: Results from the Russian drifting stations*. Berlin: Springer-Praxis.

**Grachev, AA**, **Persson, POG**, **Uttal, T**, **Akish, EA**, **Cox, CJ**, **Morris, SM**, **Fairall, CW**, **Stone, RS**, **Lesins, G**, **Makshtas, AP**, **Repina, IA.** 2017. Seasonal and latitudinal variations of surface fluxes at two Arctic terrestrial sites. *Climate Dynamics* **51**: 1793–1818. DOI: https://doi.org/10.1007/s00382-017-3983-4.

**Graham, RM**, **Rinke, A**, **Cohen, L**, **Hudson, SR**, **Walden, VP**, **Granskog, MA**, **Dorn, W**, **Kayser, M**, **Maturilli, M.** 2017. A comparison of the two Arctic atmospheric winter states observed during N-ICE2015 and SHEBA. *Journal of Geophysical Research: Atmospheres* **122**: 5716–5737. DOI: https://doi.org/10.1002/2016JD025475.

**Hankel, C**, **Tziperman, E.** 2021. The role of atmospheric feedbacks in abrupt winter Arctic sea ice loss in future warming scenarios. *Journal of Climate* **34**(11): 4435–4447. DOI: https://doi.org/10.1175/JCLI-D-20-0558.1.

**Heinemann, G**, **Schefczyk, L**, **Willmes, S**, **Shupe, MD.** 2022. Evaluation of simulations of near-surface variables using the regional climate model CCLM for the MOSAiC winter period. *Elementa: Science of the Anthropocene* **10**. DOI: https://doi.org/10.1525/elementa.2022.00033.

**Herrmannsdörfer, L**, **Müller, M**, **Shupe, MD**, **Rostosky, P.** 2023. Surface temperature comparison of the Arctic winter MOSAiC observations, ERA5 reanalysis, and MODIS satellite retrieval. *Elementa: Science of the Anthropocene* **11**(1). DOI: https://doi.org/10.1525/elementa.2022.00085.

**Huang, Y**, **Taylor, PC**, **Rose, FG**, **Rutan, DA**, **Shupe, MD**, **Webster, MA**, **Smith, MM.** 2022. Toward a more realistic representation of surface albedo in NASA CERES-derived surface radiative fluxes: A comparison with the MOSAiC field campaign. *Elementa: Science of the Anthropocene* **10**(1): 00013. DOI: https://doi.org/10.1525/elementa.2022.00013.

**Intrieri, JM**, **Fairall, CF**, **Shupe, MD**, **Persson, POG**, **Andreas, EL**, **Guest, PS**, **Moritz, RE.** 2002. An annual cycle of Arctic surface cloud forcing at SHEBA. *Journal of Geophysical Research: Oceans* **107**(C10). DOI: https://doi.org/10.1029/2000JC000439.

**Itkin, P**, **Hendricks, S**, **Webster, M**, **von Albedyll, L**, **Arndt, S**, **Divine, D**, **Jaggi, M**, **Oggier, M**, **Raphael, I**, **Ricker, R**, **Rohde, J**, **Schneebeli, M**, **Liston, GE.** 2023. Sea ice and snow characteristics from year-long transects at the MOSAiC Central Observatory. *Elementa: Science of the Anthropocene* **11**(1): 00048. DOI: https://doi.org/10.1525/elementa.2022.00048.

**Jenkins, M**, **Dai, A.** 2021. The impact of sea-ice loss on Arctic climate feedbacks and their role for Arctic amplification. *Geophysical Research Letters* **48**(15): e2021GL094599. DOI: https://doi.org/10.1029/2021GL094599.

**Jennings, KS**, **Kittel, TGF**, **Molotch, NP.** 2018. Observations and simulations of the seasonal evolution of snowpack cold content and its relation to snowmelt and the snowpack energy budget. *The Crysophere* **12**: 1595–1614. DOI: https://doi.org/10.5194/tc-12-1595-2018.

**Johnson, K**, **Giangrande, S**, **Toto, T.** 2022. Active Remote Sensing of Clouds (ARSCL) product using Ka-band ARM Zenith Radars (ARSCLKAZR1KOLLIAS). Atmospheric Radiation Measurement (ARM) User Facility. DOI: https://doi.org/10.5439/1393437.

**Jozef, GC**, **Cassano, JJ**, **Dahlke, S**, **Dice, M**, **Cox, CJ**, **de Boer, G.** 2023. Thermodynamic and kinematic drivers of atmospheric boundary layer stability in the central Arctic during the Multidisciplinary drifting Observatory for the Study of Arctic Climate (MOSAiC). *Atmospheric Chemistry and Physics* **23**: 13087–13106. DOI: https://doi.org/10.5194/acp-23-13087-2023.

**Karlsson, J**, **Svensson, G.** 2013. Consequences of poor representation of Arctic sea-ice albedo and cloud-radiation interactions in the CMIP5 model ensemble. *Geophysical Research Letters* **40**(16): 4374–4379. DOI: https://doi.org/10.1002/grl.50768.

**Karlsson, KG**, **Anttila, K**, **Trentmann, J**, **Stengel, M**, **Meirink, JF**, **Devasthale, A**, **Hanschmann, T**, **Kothe, S**, **Jaaskelainen, E**, **Sedlar, J**, **Benas, N**, **van Zadelhoff, G-J**, **Schlundt, C**, **Stein, D**, **Finkensieper, S**, **Hakansson, N**, **Hollman, R.** 2017. CLARA-A2: The second edition of the CM SAF cloud and radiation data record from 34 years of global AVHRR data. *Atmospheric Chemistry and Physics* **17**(9): 5809–5828. DOI: https://doi.org/10.5194/acp-17-5809-2017.

**Kato, S**, **Rose, FG**, **Rutan, DA**, **Thorsen, TJ**, **Loeb, NG**, **Doelling, DR**, **Huang, X**, **Smith, WL**, **Su, W**, **Ham, S-H.** 2018. Surface irradiances of edition 4.0 Clouds and the Earth's Radiant Energy System (CERES) Energy Balanced and Filled (EBAF) data product. *Journal of Climate* **31**(11): 4501–4527. DOI: https://doi.org/10.1175/JCLI-D-17-0523.1.

**Kato, S**, **Rose, FG**, **Sun-Mack, S**, **Miller, WF**, **Chen, Y**, **Rutan, DA**, **Stephens, GL**, **Loeb, NG**, **Minnis, P**, **Wielicki, BA**, **Winker, DM**, **Charlock, TP**, **Stackhouse, PWJr**, **Xu, K-M**, **Collins, WD.** 2011. Improvements of top-of-atmosphere and surface irradiance computations with CALIPSO-, CloudSat-, and MODIS-derived cloud and aerosol properties. *Journal of Geophysical Research: Atmospheres*

**116**(D19). DOI: https://doi.org/10.1029/2011JD016050.

**Khani, HM**, **Kinnard, C**, **Levesque, E.** 2022. Historical trends and projections of snow cover over the high Arctic: A review. *Water* **14**(4): 587. DOI: https://doi.org/10.3390/w14040587.

**Krishfield, RA**, **Perovich, DK.** 2005. Spatial and temporal variability of oceanic heat flux to the Arctic ice pack. *Journal of Geophysical Research: Oceans* **110**(C7): C07021. DOI:https://doi.org/10.1029/2004JC002293.

**Kwok, R**, **Untersteiner, N.** 2011. The thinning of Arctic sea ice. *Physics Today* **64**(4): 36–41. DOI: https://doi.org/10.1063/1.3580491.

**Lei, R**, **Cheng, B**, **Hoppmann, M**, **Zhang, F**, **Zuo, G**, **Hutchings, JK**, **Lin, L**, **Lan, M**, **Wang, H**, **Regnery, J**, **Krumpen, T**, **Haapala, J**, **Rabe, B**, **Perovich, DK**, **Nicolaus, M.** 2022. Seasonality and timing of sea ice mass balance and heat fluxes in the Arctic transpolar drift during 2019–2020. *Elementa: Science of the Anthropocene*. DOI: https://doi.org/10.1525/elementa.2021.000089.

**Light, B**, **Grenfell, TC**, **Perovich, DK.** 2008. Transmission and absorption of solar radiation by Arctic sea ice during the melt season. *Journal of Geophysical Research: Oceans* **113**(C3). DOI: https://doi.org/10.1029/2006JC003977.

**Light, B**, **Smith, MM**, **Perovich, DK**, **Webster, MA**, **Holland, MM**, **Linhardt, F**, **Raphael, IA**, **Clemens-Sewall, D**, **Macfarlane, AR**, **Anhaus, P**, **Bailey, DA.** 2022. Arctic sea ice albedo: Spectral composition, spatial heterogeneity, and temporal evolution observed during the MOSAiC drift. *Elementa: Science of the Anthropocene*. DOI: https://doi.org/10.1525/elementa.2021.000103.

**Maturilli, M**, **Holdridge, D**, **Dahlke, S**, **Graeser, J**, **Sommerfeld, A**, **Jaiser, R**, **Deckelmann, H**, **Schulz, A.** 2021. Initial radiosonde data from 2019-10 to 2020-09 during project MOSAiC [dataset]. Bremerhaven, Germany: Alfred Wegener Institute, Helmholtz Centre for Polar and Marine Research. PANGAEA. DOI: https://doi.org/10.1594/PANGAEA.928656.

**Maykut, GA.** 1978. Energy exchange over young sea ice in the central Arctic. *Journal of Geophysical Research: Oceans* **83**(C7): 3646–3658. DOI: https://doi.org/10.1029/JC083iC07p03646.

**Miller, NB**, **Shupe, MD**, **Cox, CJ**, **Noone, D**, **Persson, POG**, **Steffen, K.** 2017. Surface energy budget responses to radiative forcing at Summit, Greenland. *The Cryosphere* **11**: 497–516. DOI: https://doi.org/10.5194/tc-11-497-2017.

**Miller, NB**, **Shupe, MD**, **Cox, CJ**, **Walden, VP**, **Turner, DD**, **Steffen, K.** 2015. Cloud radiative forcing at Summit, Greenland. *Journal of Climate* **28**: 6267–6280. DOI: https://doi.org/10.1175/JCLI-D-15-0076.1.

**Morrison, H**, **de Boer, G**, **Feingold, G**, **Harrington, J**, **Shupe, MD**, **Sulia, K.** 2012. Resilience of persistent Arctic mixed-phase clouds. *Nature Geoscience* **5**: 11–17. DOI: https://doi.org/10.1038/NGEO1332.

**Nicolaus, M**, **Arndt, S**, **Birnbaum, G**, **Katlein, C.** 2021. Visual panoramic photographs of the surface conditions during the MOSAiC campaign 2019/20 [dataset]. PANGAEA. DOI: https://doi.org/10.1594/PANGAEA.938534.

**Nicolaus, M**, **Perovich, DK**, **Spreen, G**, **Granskog, MA**, **Albedyll, LV**, **Anhaus, P**, **Angelopoulos, M**, **Arndt, S**, **Belter, HJ**, **Bessonov, V**, **Birnbaum, G**, **Brauchle, JB**, **Calmer, R**, **Cardellach, E**, **Cheng, B**, **Clemens-Sewall, D**, **Dadic, R**, **Damm, E**, **de Boer, G**, **Demir, O**, **Dethloff, K**, **Divine, D**, **Fong, A**, **Fons, S**, **Frey, MM**, **Fuchs, N**, **Gabarró, C**, **Gerland, S**, **Gradinger, R**, **Goessling, HF**, **Haapala, J**, **Haas, C**, **Hamilton, J**, **Hannula, HR**, **Hendricks, S**, **Herber, A**, **Heuzé, C**, **Hoppmann, M**, **Høyland, KV**, **Huntemann, M**, **Hutchings, JK**, **Hwang, B**, **Itkin, P**, **Jacobi, H-W**, **Jaggi, M**, **Jutila, A**, **Kaleschke, L**, **Katlein, C**, **Kolabutin, N**, **Krampe, D**, **Kristensen, SS**, **Krumpen, T**, **Kurtz, N**, **Lampert, A**, **Lange, BA**, **Lei, R**, **Light, B**, **Linhardt, F**, **Liston, G**, **Loose, B**, **Macfarlane, AR**, **Mahmud, M**, **Matero, IO**, **Maus, S**, **Morgenstern, A**, **Naderpour, R**, **Nandan, V**, **Niubom, A**, **Oggier, M**, **Oppelt, N**, **Pätzold, F**, **Perron, C**, **Petrovsky, T**, **Pirazzini, R**, **Polashenski, C**, **Rabe, B**, **Raphael, IA**, **Regnery, J**, **Rex, M**, **Ricker, R**, **Riemann-Campe, K**, **Rinke, A**, **Rohde, J**, **Salganik, E**, **Scharien, RK**, **Schiller, M**, **Schneebeli, M**, **Semmling, M**, **Shimanchuk, E**, **Shupe, MD**, **Smith, MM**, **Smolyanitsky, V**, **Sokolov, V**, **Stanton, TP**, **Stroeve, J**, **Tavri, A**, **Thielke, L**, **Timofeeva, A**, **Tonboe, RT**, **Tsamados, M**, **Wagner, DN**, **Watkins, D**, **Webster, M**, **Wendisch, M.** 2022. Overview of the MOSAiC expedition: Snow and sea ice. *Elementa: Science of the Anthropocene* **10**(1). DOI: https://doi.org/10.1525/elementa.2021.000046.

**Nilsson, ED**, **Rannik, U**, **Hakansson, M.** 2021. Surface energy budget over the central Arctic Ocean during late summer and early freeze-up. *Journal of Geophysical Research: Atmospheres* **106**: 32187–32205.

**Nixdorf, U**, **Dethloff, K**, **Rex, M**, **Shupe, M**, **Sommerfeld, A**, **Perovich, D**, **Nicolas, M**, **Heuze, C**, **Rabe, B**, **Loose, B**, **Damm, E**, **Gradinger, R**, **Fong, A**, **Maslowski, W**, **Rinke, A**, **Kwok, R**, **Spreen, G**, **Wendisch, M**, **Herber, A**, **Hirsekorn, M**, **Mohaupt, V**, **Frickenhaus, S**, **Immerz, A**, **Weiss-Tuider, K**, **Koenig, B**, **Mengedoht, D**, **Regnery, J**, **Gerchow, P**, **Ransby, D**, **Krumpen, T**, **Morgenstern, A**, **Haas, C**, **Kanzow, T**, **Rack, FR**, **Saitzev, V**, **Sokolov, V**, **Makarov, A**, **Schwarze, S**, **Wunderlich, T**, **Wurr, K**, **Boetius, A.** 2021. MOSAiC extended acknowledgement. Zenodo. DOI: https://doi.org/10.5281/zenodo.5179738.

**Perovich, D**, **Raphael, I**, **Moore, R**, **Clemens-Sewall, D**, **Lei, R**, **Sledd, A**, **Polashenski, C.** 2023. Sea ice heat and mass balance measurements from four autonomous buoys during the MOSAiC drift campaign. *Elementa: Science of the Anthropocene* **11**(1): 00017. DOI: https://doi.org/10.1525/elementa.2023.00017.

**Perovich, DK**, **Light, B**, **Smith, MM**, **Webster, M**, **Holland, MM**, **Clemens-Sewall, D**, **Raphael, IA**, **Polashenski, C**, **Barrett, AP**, **Cox, CJ**, **Itkin, P**, **Linhardt, F**, **Macfarlane, AR**, **Nicolaus, M**, **Oppelt, N**, **Shupe, MD**, **Stroeve, J**, **Tao, R.** 2025. Theoretical estimates of light transmittance at the MOSAiC Central Observatory. *Elementa: Science of the Anthropocene* **13**(1). DOI: https://doi.org/10.1525/elementa.2024.00076.

**Persson, POG.** 2012. Onset and end of the summer melt season over sea ice: Thermal structure and surface energy perspective from SHEBA. *Climate Dynamics* **39**: 1349–1371. DOI: https://doi.org/10.1007/s00382-011-1196-9.

**Persson, POG**, **Fairall, CW**, **Andreas, EL**, **Guest, PS**, **Perovich, DK.** 2002. Measurements near the Atmospheric Surface Flux Group tower at SHEBA: Near-surface conditions and surface energy budget. *Journal of Geophysical Research: Oceans* **107**. DOI: https://doi.org/10.1029/2000JC000705.

**Persson, POG**, **Shupe, MD**, **Perovich, D**, **Solomon, A.** 2017. Linking atmospheric synoptic transport, cloud phase, surface energy fluxes, and sea-ice growth: Observations of midwinter SHEBA conditions. *Climate Dynamics* **49**: 1341–1364. DOI: https://doi.org/10.1007/s00382-016-3383-1.

**Pithan, F**, **Athanase, M**, **Dahlke, S**, **Sanchez-Benitez, A**, **Shupe, MD**, **Sledd, A**, **Streffing, J**, **Svensson, G**, **Jung, T.** 2023. Nudging allows direct evaluation of coupled climate models with in situ observations: A case study from the MOSAiC expedition. *Geoscientific Model Development* **16**(7): 1857–1873. DOI: https://doi.org/10.5194/gmd-16-1857-2023.

**Pithan, F**, **Medeiros, B**, **Mauritsen, T.** 2014. Mixed-phase clouds cause climate model biases in Arctic wintertime temperature inversions. *Climate Dynamics* **43**: 289–303.

**Previdi, M**, **Smith, KL**, **Polvani, LM.** 2021. Arctic amplification of climate change: A review of underlying mechanisms. *Environmental Research Letters* **16**(9): 093003. DOI: https://doi.org/10.1088/1748-9326/ac1c29.

**Rabe, B**, **Cox, CJ**, **Fang, Y-C**, **Goessling, H**, **Granskog, MA**, **Hoppmann, M**, **Hutchings, JK**, **Krumpen, T**, **Kuznetsov, I**, **Lei, R**, **Li, T**, **Maslowski, W**, **Nicolaus, M**, **Perovich, D**, **Persson, O**, **Regnery, J**, **Rigor, I**, **Shupe, MD**, **Sokolov, V**, **Spreen, G**, **Stanton, T**, **Watkins, DM**, **Blockley, E**, **Jakob Buenger, HJ**, **Cole, S**, **Fong, A**, **Haapala, J**, **Heuze, C**, **Hoppe, CJM**, **Janout, M**, **Jutila, A**, **Katlein, C**, **Krishfield, R**, **Lin, L**, **Ludwig, V**, **Morgenstern, A**, **O'Brien, J**, **Zurita, AQ**, **Rackow, T**, **Riemann-Campe, K**, **Rohde, J**, **Shaw, W**, **Smolyanitsky, V**, **Solomon, A**, **Sperling, A**, **Tao, R**, **Toole, J**, **Tsamados, M**, **Zhu, J**, **Zuo, G.** 2024. The MOSAiC Distributed Network: Observing the coupled Arctic system with multidisciplinary, coordinated platforms. *Elementa: Science of the Anthropocene* **12**(1): 00103. DOI: https://doi.org/10.1525/elementa.2023.00103.

**Raphael, IA**, **Perovich, DK**, **Polashenski, CM**, **Clemens-Sewall, D**, **Itkin, P**, **Lei, R**, **Nicolaus, M**, **Regnery, J**, **Smith, MM**, **Webster, M**, **Jaggi, M.** 2024. Sea ice mass balance during the MOSAiC drift experiment: Results from manual ice and snow thickness gauges. *Elementa: Science of the Anthropocene* **12**(1): 00040. DOI: https://doi.org/10.1525/elementa.2023.00040.

**Riihelä, A**, **Key, JR**, **Meirink, JF**, **Munneke, PK**, **Palo, T**, **Karlsson, K-G.** 2017. An intercomparison and validation of satellite-based surface radiative energy flux estimates over the Arctic. *Journal of Geophysical Research: Atmospheres* **122**(9): 4829–4848. DOI: https://doi.org/10.1002/2016JD026443.

**Ruffieux, D**, **Persson, POG**, **Fairall, CW**, **Wolfe, DE.** 1995. Ice pack and lead surface energy budgets during LEADEX 1992. *Journal of Geophysical Research: Oceans* **100**(C3): 4593–4612. DOI: https://doi.org/10.1029/94JC02485.

**Schnierstein, N**, **Chylik, J**, **Shupe, MD**, **Neggers, RAJ.** 2024. Standardized daily high-resolution Large-Eddy Simulations of the Arctic boundary layer and clouds during the complete *MOSAiC* drift. *Journal of Advances in Modeling Earth Systems* **16**: e2024MS004296. DOI: https://doi.org/10.1029/2024MS004296.

**Sedlar, J**, **Tjernström, M**, **Mauritsen, T**, **Shupe, MD**, **Brooks, IM**, **Persson, POG**, **Birch, CE**, **Leck, C**, **Sirevaag, A**, **Nicolaus, M.** 2011. A transitioning Arctic surface energy budget: The impacts of solar zenith angle, surface albedo and cloud radiative forcing. *Climate Dynamics* **37**(7–8): 1643–1660. DOI: https://doi.org/10.1007/s00382-010-0937-5.

**Sedlar, J**, **Tjernström, M**, **Rinke, A**, **Orr, A**, **Cassano, J**, **Fettweis, X**, **Heinemann, G**, **Seefeldt, M**, **Solomon, A**, **Matthes, H**, **Phillips, T**, **Webster, S.** 2020. Confronting Arctic troposphere, clouds, and surface energy budget representations in Regional Climate Models with observations. *Journal of Geophysical Research: Atmospheres* **125**(6): e2019JD031783. DOI: https://doi.org/10.1029/2019JD031783.

**Shupe, MD.** 2011. Clouds at Arctic atmospheric observatories. Part II: Thermodynamic phase characteristics. *Journal of Applied Meteorology and Climatology* **50**: 645–661. DOI: https://doi.org/10.1175/2010JAMC2468.1.

**Shupe, MD.** 2022. ShupeTurner cloud microphysics product [dataset]. ARM Mobile Facility (MOS) MOSAiC (Drifting Obs—Study of Arctic Climate). DOI: https://doi.org/10.5439/1871015.

**Shupe, MD**, **Intrieri, JM.** 2004. Cloud radiative forcing of the Arctic surface: The influence of cloud properties, surface albedo, and solar zenith angle. *Journal of Climate* **17**: 616–628. DOI: https://doi.org/10.1175/1520-0442(2004)017<0616:CRFOTA>2.0.CO;2.

**Shupe, MD**, **Rex, M**, **Blomquist, B**, **Persson, POG**, **Schmale, J**, **Uttal, T**, **Althausen, D**, **Angot, H**, **Archer, S**, **Bariteau, L**, **Beck, I**, **Bilberry, J**, **Bucci,**

**S**, **Buck, C**, **Boyer, M**, **Brasseur, Z**, **Brooks, IM**, **Calmer, R**, **Cassano, J**, **Castro, V**, **Chu, D**, **Costa, D**, **Cox, C**, **Creamean, J**, **Crewell, S**, **Dahlke, S**, **Damm, E**, **de Boer, G**, **Deckelmann, H**, **Dethloff, K**, **Dütsch, M**, **Ebell, K**, **Ehrlich, A**, **Ellis, J**, **Engelmann, R**, **Fong, AA**, **Frey, MM**, **Gallagher, MR**, **Ganzeveld, L**, **Gradinger, R**, **Graeser, J**, **Greenamyer, V**, **Griesche, H**, **Griffiths, S**, **Hamilton, J**, **Heinemann, G**, **Helmig, D**, **Herber, A**, **Heuzé, C**, **Hofer, J**, **Houchens, T**, **Howard, D**, **Inoue, J**, **Jacobi, HW**, **Jaiser, R**, **Jokinen, T**, **Jourdan, O**, **Jozef, G**, **King, W**, **Kirchgaessner, A**, **Klingebiel, M**, **Krassovski, M**, **Krumpen, T**, **Lampert, A**, **Landing, W**, **Laurila, T**, **Lawrence, D**, **Lonardi, M**, **Loose, B**, **Lüpkes, C**, **Maahn, M**, **Macke, A**, **Maslowski, W**, **Marsay, C**, **Maturilli, M**, **Mech, M**, **Morris, S**, **Moser, M**, **Nicolaus, M**, **Ortega, P**, **Osborn, J**, **Pätzold, F**, **Perovich, D**, **Petäjä, T**, **Pilz, C**, **Pirazzini, R**, **Posman, K**, **Powers, H**, **Pratt, K**, **Preußer, A**, **Quéléver, L**, **Radenz, M**, **Rabe, B**, **Rinke, A**, **Sachs, T**, **Schulz, A**, **Siebert, H**, **Silva, T**, **Solomon, A**, **Sommerfeld, A**, **Spreen, G**, **Stephens, M**, **Stohl, A**, **Svensson, G**, **Uin, J**, **Viegas, J**, **Voigt, C**, **von der Gathen, P**, **Wehner, B**, **Welker, JM**, **Wendisch, M**, **Werner, M**, **Xie, Z**, **Yue, F.** 2022. Overview of the MOSAiC expedition: Atmosphere. *Elementa: Science of the Anthropocene* **10**(1): 00060. DOI: https://doi.org/10.1525/elementa.2021.00060.

**Shupe, MD**, **Rex, M**, **Dethloff, K**, **Damm, E**, **Fong, AA**, **Gradinger, R**, **Heuze, C**, **Loose, B**, **Makarov, A**, **Maslowski, W**, **Nicolaus, M**, **Perovich, D**, **Rabe, B**, **Rinke, A**, **Sokolov, V**, **Sommerfeld, A.** 2020. The MOSAiC expedition: A year drifting with the Arctic sea ice, in Thoman, RL, Richter-Menge, J, Druckenmiller, ML eds., *Arctic report card 2020*. DOI: https://doi.org/10.25923/9g3v-xh92.

**Shupe, MD**, **Turner, DD**, **Zwink, A**, **Theiman, MM**, **Mlawer, EJ**, **Shippert, T.** 2015. Deriving Arctic cloud microphysics at Barrow, Alaska: Algorithms, results, and radiative closure. *Journal of Applied Meteorology and Climatology* **54**: 1675–1689. DOI: https://doi.org/10.1175/JAMC-D-15-0054.1.

**Sivaraman, C**, **Flynn, D**, **Riihimaki, L**, **Comstock, J**, **Zhang, D.** 2022. Cloud mask from Micropulse Lidar (30SMPLCMASK1ZWANG) [dataset]. Atmospheric Radiation Measurement (ARM) User Facility. DOI: https://doi.org/10.5439/1508389.

**Sledd, A**, **Shupe, M**, **Solomon, A**, **Cox, C**, **Perovich, D**, **Lei, R.** 2023. Winter snow and sea ice thermal conductivity, density, and conductive heat flux profiles from the Multidisciplinary drifting Observatory for the Study of Arctic Climate (MOSAiC) expedition, central Arctic, October 2019–March 2020 [dataset]. Arctic Data Center. DOI: https://doi.org/10.18739/A2NK3669K.

**Sledd, A**, **Shupe, MD**, **Solomon, A**, **Cox, CJ.** 2025. Surface energy balance responses to radiative forcing in the Central Arctic from MOSAiC and models. *Journal of Geophysical Research: Atmospheres* **130**: e2024JD042578. DOI: https://doi.org/10.1029/2024JD042578.

**Sledd, A**, **Shupe, MD**, **Solomon, A**, **Cox, CJ**, **Perovich, D**, **Lei, R.** 2024. Snow thermal conductivity and conductive flux in the Central Arctic: Estimates from observations and implications for models. *Elementa: Science of the Anthropocene* **12**(1): 00086. DOI: https://doi.org/10.1525/elementa.2023.00086.

**Solomon, A**, **Shupe, MD**, **Svensson, G**, **Barton, NP**, **Batrak, Y**, **Bazile, E**, **Day, JJ**, **Doyle, JD**, **Frank, HP**, **Keeley, S**, **Remes, T**, **Tolstykh, M.** 2023. The winter central Arctic surface energy budget: A model evaluation using observations from the MOSAiC campaign. *Elementa: Science of the Anthropocene* **11**(1): 00104. DOI: https://doi.org/10.1525/elementa.2022.00104.

**Sorteberg, A**, **Kattsov, V**, **Walsh, JE**, **Pavlova, T.** 2007. The Arctic surface energy budget as simulated with IPCC AR4 AOGCMs. *Climate Dynamics* **29**: 131–156.

**Stapf, J**, **Ehrlich, A**, **Wendisch, M.** 2021. Influence of thermodynamic state changes on surface cloud radiative forcing in the Arctic: A comparison of two approaches using data from AFLUX and SHEBA. *Journal of Geophysical Research: Atmospheres* **126**: e2020JD033589. DOI: https://doi.org/10.1029/2020JD033589.

**Stramler, K**, **Del Genio, AD**, **Rossow, WB.** 2011. Synoptically driven Arctic winter states. *Journal of Climate* **24**(6): 1747–1762. DOI: https://doi.org/10.1175/2010JCLI3817.1.

**Stuecker, MF**, **Bitz, CM**, **Armour, KC**, **Proistosescu, C**, **Kang, SM**, **Xie, S-P**, **Kim, D**, **McGregor, S**, **Zhang, W**, **Zhao, S**, **Cai, W**, **Dong, Y**, **Jin, F-F.** 2018. Polar amplification dominated by local forcing and feedbacks. *Nature Climate Change* **8**: 1076–1081.

**Svensson, G**, **Karlsson, J.** 2011. On the Arctic wintertime climate in global climate models. *Journal of Climate* **24**(22): 5757–5771. DOI: https://doi.org/10.1175/2011JCLI4012.1.

**Svensson, G**, **Murto, S**, **Shupe, MD**, **Pithan, F**, **Magnusson, L**, **Day, JJ**, **Doyle, JD**, **Renfrew, IA**, **Spengler, T**, **Vihma, T.** 2023. Warm air intrusions reaching the MOSAiC expedition in April 2020—The YOPP targeted observing period (TOP). *Elementa: Science of the Anthropocene* **11**(1). DOI: https://doi.org/10.1525/elementa.2023.00016.

**Tjernström, M**, **Sedlar, J**, **Shupe, MD.** 2008. How well do regional climate models reproduce radiation and clouds in the Arctic? An evaluation of ARCMIP simulations. *Journal of Applied Meteorology and Climatology* **47**: 2405–2422.

**Turner, DD**, **Clough, SA**, **Liljegren, JC**, **Clothiaux, EE**, **Cady-Pereira, KE**, **Gaustad, KL.** 2007. Retrieving liquid water path and precipitable water vapor from the Atmospheric Radiation Measurement (ARM) microwave radiometers. *IEEE Transactions in Geosciences and Remote Sensing* **45**(11): 3680–3690. DOI: https://doi.org/10.1109/TGRS.2007.903703.

**Walden, VP**, **Hudson, SR**, **Cohen, L**, **Murphy, SY**, **Granskog, MA.** 2017. Atmospheric components of

the surface energy budget over young sea ice: Results from the N-ICE2015 campaign. *Journal of Geophysical Research: Atmospheres* **122**(16): 8427–8446. DOI: https://doi.org/10.1002/2016JD026091.

**Walsh, JE**, **Chapman, WL.** 1998. Arctic cloud–radiation–temperature associations in observational data and atmospheric reanalysis. *Journal of Climate* **11**(11): 3030–3045.

**Wang, M**, **Johnson, K**, **Giangrande, S.** 2022. Marine W-band ARM Cloud Radar, Active Remote Sensing of Clouds (ARSCLWACR1KOLLIASSHP) [dataset]. Atmospheric Radiation Measurement (ARM) User Facility. DOI: https://doi.org/10.5439/1823070.

**Webster, MA**, **Holland, M**, **Wright, NC**, **Hendricks, S**, **Hutter, N**, **Itkin, P**, **Light, B**, **Linhardt, F**, **Perovich, DK**, **Raphael, IA**, **Smith, MM**, **von Albedyll, L**, **Zhang, J.** 2022. Spatiotemporal evolution of melt ponds on Arctic sea ice: MOSAiC observations and model results. *Elementa: Science of the Anthropocene* **10**(1). DOI: https://doi.org/10.1525/elementa.2021.000072.

**Wendisch, M**, **Bruckner, M**, **Crewell, S**, **Ehrlich, A**, **Notholt, J**, **Lupkes, C**, **Macke, A**, **Burrows, JP**, **Rinke, A**, **Quaas, J**, **Maturilli, M**, **Schemann, V**, **Shupe, MD**, **Akansu, EF**, **Barientos-Velasco, C**, **Barfuss, K**, **Blechschmidt, A-M**, **Block, K**, **Bougoudis, I**, **Bozem, H**, **Bockmann, C**, **Bracher, A**, **Bresson, H**, **Bretschneider, L**, **Buschmann, M**, **Chechin, D**, **Chylik, J**, **Dahlke, S**, **Deneke, H**, **Dethloff, K**, **Donth, T**, **Dorn, W**, **Dupuy, R**, **Ebell, K**, **Egerer, U**, **Engelmann, R**, **Eppers, O**, **Gerdes, R**, **Gierens, R**, **Gorodetskaya, IV**, **Gottschalk, M**, **Griesche, H**, **Gryanik, VM**, **Handorf, D**, **Harm-Altstadter, B**, **Hartmann, J**, **Hartmann, M**, **Heinold, B**, **Herber, A**, **Herrmann, H**, **Heygster, G**, **Hoeschel, I**, **Hofmann, Z**, **Hoelemann, J**, **Huenerbein, A**, **Jafariserajehlou, S**, **Jaekel, E**, **Jacobi, C**, **Janout, M**, **Jansen, F**, **Jourdan, O**, **Juranyi, Z**, **Kalesse-Los, H**, **Kanzow, T**, **Kaethner, R**, **Kliesch, L**, **Klingebiel, M**, **Knudsen, E**, **Kovacz, T**, **Koertke, W**, **Krampe, D**, **Kretzschmar, J**, **Kreyling, D**, **Kulla, B**, **Kunkel, D**, **Lampert, A**, **Lauer, M**, **Lelli, L**, **von Lerber, A**, **Linke, O**, **Loehnert, U**, **Lonardi, M**, **Losa, SN**, **Losch, M**, **Maahn, M**, **Mech, M**, **Mei, L**, **Mertes, S**, **Metzner, E**, **Mewes, D**, **Michaelis, J**, **Mioche, G**, **Moser, M**, **Nakoudi, K**, **Neggers, R**, **Neuber, R**, **Nomokonova, T**, **Oelker, J**, **Papakonstantinou-Presvelou, I**, **Patzold, R**, **Pefanis, V**, **Pohl, C**, **van Pinxteren, M**, **Radovan, A**, **Rhein, M**, **Rex, M**, **Richter, A**, **Risse, N**, **Ritter, C**, **Rostosky, P**, **Rosanov, VV**, **Ruiz Donoso, E**, **Saavedra-Garfias, P**, **Salzmann, M**, **Schacht, J**, **Schaefer, M**, **Schneider, J**, **Schnierstein, N**, **Seifert, P**, **Seo, C**, **Siebert, H**, **Soppa, MA**, **Spreen, G**, **Stachlewska, IS**, **Stapf, J**, **Stratmann, F**, **Tegen, I**, **Viceto, C**, **Voigt, C**, **Vountas, M**, **Walbroel, A**, **Walter, M**, **Wehner, B**, **Wex, H**, **Zanatta, M**, **Zeppenfeld, S.** 2022. Atmospheric and surface processes, and feedback mechanisms determining arctic amplification: A review of first results and prospects of the $(AC)^3$ project. *Bulletin of the American Meteorological Society* **104**(1): E208–E242. DOI: https://doi.org/10.1175/BAMS-D-21-0218.1.

**Yu, Q**, **Wu, B**, **Zhang, W.** 2024. The atmospheric connection between the Arctic and Eurasia is underestimated in simulations with prescribed sea ice. *Communications Earth and Environment* **5**: 435. DOI: https://doi.org/10.1038/s43247-024-01605-2.

**Zhang, D.** 2022. MWR retrievals (MWRRET1LILJCLOU) [dataset]. Atmospheric Radiation Measurement (ARM) User Facility. DOI: https://doi.org/10.5439/1027369.

**Zhang, D**, **Ermold, B**, **Morris, V.** 2022. Ceilometer (CEIL) [dataset]. Atmospheric Radiation Measurement (ARM) User Facility. DOI: https://doi.org/10.5439/1181954.

**Zhang, R**, **Wang, H**, **Fu, Q**, **Rasch, PJ**, **Wu, M**, **Maslowski, W.** 2021. Understanding the cold season Arctic surface warming trend in recent decades. *Geophysical Research Letters* **48**(19): e2021GL094878. DOI: https://doi.org/10.1029/2021GL094878.

**Zhang, Y-C**, **Rossow, WB**, **Lacis, AA**, **Oinas, V**, **Mishchenko, MI.** 2004. Calculation of radiative fluxes from the surface to top of atmosphere based on ISCCP and other global data sets: Refinements of the radiative transfer model and the input data. *Journal of Geophysical Research: Atmospheres* **109**(D19). DOI: https://doi.org/10.1029/2003JD004457.

**Zhang, Z-L**, **Hui, F-M**, **Vihma, T**, **Granskog, MA**, **Cheng, B**, **Chen, Z-Q**, **Cheng, X.** 2023. On the turbulent heat fluxes: A comparison among satellite-based estimates, atmospheric reanalyses, and *in-situ* observations during the winter climate over Arctic sea ice. *Advances in Climate Change Research* **14**(3): 347–362. DOI: https://doi.org/10.1016/j.accre.2023.04.004.

**How to cite this article:** Shupe, MD, Persson, POG, Cox, CJ, Gallagher, MR, Solomon, A, Sledd, A, Blomquist, B, Brooks, IM, Costa, D, Osborn, J, Perovich, D, Riihimaki, LD, Uttal, T. 2026. The two radiative states of the Arctic atmosphere and their impacts on the surface energy budget of sea ice. *Elementa: Science of the Anthropocene* 14(1). DOI: https://doi.org/10.1525/elementa.2025.00100

**Domain Editor-in-Chief:** Detlev Helmig, Boulder AIR LLC, Boulder, CO, USA

**Guest Editor:** Zoe Courville, U.S. Army Engineer Research and Development Center Cold Regions Research and Engineering Laboratory, Dartmouth, Hanover, NH, USA

**Knowledge Domain:** Atmospheric Science

**Part of an Elementa Special Feature:** The Multidisciplinary Drifting Observatory for the Study of Arctic Climate (MOSAiC)

**Published:** April 15, 2026 **Accepted:** January 23, 2026 **Submitted:** September 27, 2025



ELEMENTA Science of the Anthropocene

*Elem Sci Anth* is a peer-reviewed open access journal published by University of California Press.

OPEN ACCESS